MODELING RF HEATING OF ACTIVE IMPLANTABLE MEDICAL DEVICES DURING MRI USING SAFETY INDEX

A THESIS
SUBMITTED TO THE DEPARTMENT OF ELECTRICAL AND
ELECTRONICS ENGINEERING
AND THE INSTITUTE OF ENGINEERING AND SCIENCES
OF BILKENT UNIVERSITY
IN PARTIAL FULLFILMENT OF THE REQUIREMENTS
FOR THE DEGREE OF
MASTER OF SCIENCE

By
Halise Irak
August 2007

I certify that I have read this thesis and that in my opinion it is fully adequate, in scope and in quality, as a thesis for the degree of Master of Science.

Prof. Dr. Ergin Atalar (Supervisor)

I certify that I have read this thesis and that in my opinion it is fully adequate, in scope and in quality, as a thesis for the degree of Master of Science.

Prof. Dr. Nevzat Gençer

I certify that I have read this thesis and that in my opinion it is fully adequate, in scope and in quality, as a thesis for the degree of Master of Science.

Assist. Prof. Dr. Vakur Ertürk

Approved for the Institute of Engineering and Sciences:

Prof. Dr. Mehmet B. Baray
Director of Institute of Engineering and Sciences

ABSTRACT

MODELING RF HEATING OF ACTIVE IMPLANTABLE MEDICAL DEVICES DURING MRI USING SAFETY INDEX

Halise Irak
M.S. in Electrical and Electronics Engineering
Supervisor: Prof. Dr. Ergin Atalar
August 2007

Magnetic Resonance Imaging (MRI) is known as a safe imaging modality that can be hazardous for patients with active implantable medical devices, such as a pacemakers or deep brain stimulators. The primary reason for that is the radio frequency (RF) heating at the tips of the implant leads. In the past, this problem has been analyzed with phantom, animal and human experiments. The amount of temperature rise at the lead tip of these implants, however, has not been theoretically analyzed. In this thesis, a simple approximate formula for the *safety index* of implants, which is the temperature increase at the implant lead tip per unit deposited power in the tissue without the implant in place, was derived.

For that purpose, an analytical quadrature birdcage coil model was developed and the longitudinal incident electric field distribution inside the body was formularized as follows:

$$E_z(R) = -\omega \mu H_- \mathrm{R}$$

in which ω is the angular frequency, μ is the magnetic permeability of the tissue, H_- is the left hand rotating component of the RF magnetic field and R is the radial distance from the center of the body. This formula was examined by simulations and phantom experiments. The analytical, simulation and experimental results of that model are in good agreement.

Then, depending on the quadrature birdcage coil model safety index (SI) formula for active implants with short leads was derived as shown below:

$$SI = \frac{\Delta T_{\max}}{SAR_{\text{peak}}} = \frac{1}{2\alpha c_t R_b^2}\left|Rl + Ae^{j\theta}\right|^2 f(Dv)$$

where ΔT_{max} is the maximum temperature increase in the tissue, SAR_{peak} is the maximum deposited power in the body when there is no implant in the body, α is the diffusivity of the tissue, c_t is the heat capacity of the tissue, R_b is radius of the body, R is the radial distance from the center of the body, l is the length of the implant lead, A is the area of the curvature of the lead, θ is the angle that curvature of the implant makes with the radial axis, and $f(Dv)$ is the perfusion correction factor, which is function of the diameter of the electrode and perfusion. The safety index formula was tested by simulations. Simulation results showed that the theoretical safety index formula approximates and identifies the RF heating problem of active implants with short leads accurately.

The safety index formula derived in this thesis is valid for only short wires. However, the formulation for long wires is currently under investigation. Despite the fact that the results obtained for short leads can not be generalized for the safety of patients with active implants, it is believed that this study is the first step towards safety of these patients. Using safety index as a measure of safety is very beneficial to ensure the safety of patients with active implants. Because, it uses the MR scanner-estimated deposited power that does not take the existence of the implant in the patient body into account. This formulation is the first study illustrating the advantage of the safety index metric for RF heating studies of active implants.

Keywords: MRI, RF heating, Active Implants, RF Safety, Safety Index, Quadrature Birdcage Coil

ÖZET

VÜCUDA TAKILABİLEN TIBBİ ELEKTRONİK ÜRETEÇLERİN MR GÖRÜNTÜLENMESİNİN GÜVENLİK İNDEKSİ KULLANILARAK RADYO FREKANS MODELLENDİRİLMESİ

Halise Irak
Elektrik ve Elektronik Mühendisliği Bölümü Yüksek Lisans
Tez Yöneticisi: Prof. Dr. Ergin Atalar
Ağustos 2005

MR görüntüleme güvenli bir görüntüleme tekniği olarak bilinmektedir. Fakat kalp pili ve derin beyin uyarıcıları gibi tıbbi elektronik üreteçler taşıyan hastalar için tehlikeli olabilir. Bunun temel nedeni elektronik üreteçlerin kablolarında bulunan elektrotların radyo frekans (RF) dalgalar nedeniyle ısınmasıdır. Geçmişte bu problem insan modelleri, hayvanlar ve insanlar üzerinde yapılan deneylerle analiz edilmiştir. Ancak bu üreteçlerin elektrotlarında meydana gelen sıcaklık artışı teorik olarak analiz edilmemiştir. Bu tezde, üreteçlerin *güvenlik indeks*'ini yaklaşık olarak hesaplayan basit bir formül türetilmiştir. *Güvenlik indeks*'i vücutta üreteç varken meydana gelen sıcaklık artışının, üreteç olmadığı zaman dokuda depolanan birim enerjiye oranı olarak tanımlanmaktadır.

Bu amaçla, analitik çeyrek evre kuş kafesi sargı modeli geliştirilmiş ve vücuda boylamsal düşen elektrik alan dağılımı aşağıdaki gibi formülleştirilmiştir:

$$E_z(R) = -\omega \mu H_- \mathrm{R}$$

bu formülde ω açısal frekansı, μ dokunun manyetik geçirgenliğini, H_- RF manyetik alanın sol el kuralına göre dönen bileşenini ve R vücudun merkezinden olan radyal uzaklığı simgelemektedir. Bu formül simulasyonlar ve insan modeli deneyleriyle sorgulanmıştır. Bu modelin analitik, simulasyon ve deney sonuçları büyük oranda uyuşmaktadır.

Bu formülasyona dayanarak kısa kablolu elektronik üreteçlerin Güvenlik İndeks (Gİ) formülü aşağıdaki gibi türetilmiştir:

$$SI = \frac{\Delta T_{\max}}{SAR_{\mathrm{peak}}} = \frac{1}{2\alpha c_t R_b^2} \left| Rl + Ae^{j\theta} \right|^2 f(Dv)$$

Bu formülde ΔT_{max} dokudaki maksimum sıcaklık artışını, SAR_{peak} vücutta üreteç yokken biriken maksimum gücü, α dokudaki yayılma gücünü, c_t dokunun sıcaklık kapasitesini, R_b vücudun yarı çapını, R vücudun merkezinden olan radial uzaklığı, *l* üretecin kablo uzunluğunu, A kablonun eğrilik alanını, θ üretecin kablo eğrisinin radyal eksenle yaptığı açıyı ve *f(Dv)* elektrot çapına ve perfüzyona bağlı olan perfüzyon düzeltme faktörünü simgelemektedir. Güvenlik indeks formülü simulasyonlarla test edilmiştir. Simulasyon sonuçları teorik güvenlik indeks formülünün yaklaşık olarak kısa kablolu üreteçlerin RF ısınma problemini açıkladığını göstermiştir.

Bu tezde türetilen güvenlik indeks formülü kısa kablolar için geçerlidir. Uzun kablolar için olan formül üzerinde çalışmalar devam etmektedir. Kısa kablolarla elde edilen sonuçlar üreteçleri olan hastaların güvenliği için genellenemese de, inanıyoruz ki bu çalışma bu hastaların güvenliği için yapılacak olan çalışmalara öncü nitelik taşımaktadır. Güvenlik indeksini güvenlik ölçütü olarak kullanmak, MR tarayıcının tahmin ettiği vücutta üreteç yokken depolanan gücü kullanarak hesaplandığı için elektronik üreteçleri olan hastaların güvenliğini sağlamak açısından oldukça faydalıdır. Bu formülasyon güvenlik indeksini güvenlik ölçütü olarak almanın ne kadar faydalı olduğunu göstermek açısından elektronik üreteçlerin RF ısınması üzerine yapılan ilk çalışmadır.

Anahtar Kelimeler: MR Görüntüleme, RF Isınma, Elektronik Üreteçler, RF Güvenlik, Güvenlik İndeksi, Çeyrek Evre Kuş Kafesi Sargısı.

To my father Hamdullah and Prof. Ergin Atalar

for giving me a chance.

Table of Contents

List of Figures

List of Tables

Chapter 1

Introduction

1.1 Motivation and Literature Survey

There is an increasing demand for MRI exams of patients with active implantable medical devices (AIMD) such as pacemakers and deep brain stimulators. Unfortunately, these patients are barred from MRI exams primarily due to the possibility of hazardous RF heating at the lead tips of the implants. Despite the fact that most of the studies on the RF heating of implants are limited by testing of leads with phantom [1-3], animal [4] and human [5] experiments, there are a small number of quantitative studies [6-8]. These assessments focus on the heating of a straight wire as a good approximation for the RF heating of an implant with insulation [6], without insulation[6, 7], and insulation with exposed tips [7, 8]. Furthermore, the effects of loops constructed by leads were computed [9] and observed experimentally with phantom experiments [3, 10-12]. In the literature, there is no study with the aim of finding an analytical formula for the problem of AIMD heating. Such formula will enable us 1) to understand the parameters affecting the tip heating; 2) to determine the maximum power that can be safely applied during an MRI examination; and 3) to develop novel and effective methods to reduce coupling between AIMD and the MRI scanner.

It was reported [13] that just after an MRI examination of the head at 1 Tesla (T), a 73-year-old patient with bilateral implanted deep brain stimulator electrodes for Parkinson disease showed dystonic and partially ballistic movements of the left leg. Despite the fact that MR imaging of patients with deep brain stimulators was performed many times at 1.5 T with no side effects before this incident, this incident shows that the generalization of the same conditions even at lower field strengths, i.e. 1 T, can be dangerous. Consequently, it is suggested [14-17] that each MRI system and update of the same system needs a specific safety regulation assessed with a preclinical study for the RF heating of the specific implant leads during MRI examinations. According to these studies [14-18], since MRI scanner calculated SAR does not take the existence of the active implants in the body into account, it is not reliable to use it for ensuring the safety of patients. Therefore, safety recommendations developed for a certain system, i.e. type of implant, body coil, MRI system and field strength, especially when the estimated SAR of the system is concerned may not be implemented across different MRI systems.

As it is seen, there is a doubt in the literature for the reliability of SAR (when there is an implant, people do not speak much on SAR but they focus on temperature) for the RF safety of patients with active implant. All of these controversies imply that all parameters of the RF heating problem should be clearly determined and put in a comprehensible form such that it becomes easier to develop universal RF safety limits. To achieve such practical format, the RF heating of active implants should be analytically analyzed. Considering the variety of the MRI scanners and active implants, and how regularly they are updated, it is more realistic to search for a consistent solution in which the type of the MRI system is not a parameter.

In this study, the MRI-related RF heating problem of active implantable medical devices (AIMDs) with a single short lead considering the curvature of the lead was theoretically analyzed at 1.5 T. The *safety index* [6] of active implants; the temperature rise at the implant lead tip per unit deposited power in the tissue without the implant in place, was also formulated. For that purpose, an active implant was placed in an infinitely long cylindrical human body model. It is assumed to lie coaxial with the transmit body coil. Then, the incident electric field on the implant was analytically found under the quasistatic assumption.

Next, the induced current, the SAR amplification and the resultant temperature increase in the tissue was formulated in terms of the electrical and thermal characteristics of the tissue and the characteristics of the implant configuration such as radius of the tip, length of the lead, area of the lead curvature and the position of the implant. Finally, the resultant temperature at the tip was normalized with the peak SAR in the body to find the safety index of the active implant. As a result of this analysis, it was aimed to explain how important and practical to use *safety index* metric in order to ensure the RF heating safety of active implants. Thus, this study shows that RF heating can be analytically identified and the safety index formula helps the standardization of the MRI-related RF heating problem. Besides, since it is required to calculate the safety index, scanner estimated SAR was shown to be vital for the RF safety of patients with active implants.

1.2 The Objective and Scope of the Thesis

In this thesis, an analytical analysis of the RF heating problem of AIMDs was done with the purpose of deriving a general formulation for the safety index of AIMDs. After calculating the induced electrical field on the cylindrical human model, the amplified absorbed power at the tip of the AIMD was found. Next, the temperature increase in the tissue was studied and finally the safety index of the AIMD was calculated by normalizing the temperature rise with respect to the absorbed power in the tissue when the AIMD is not in place.

This thesis has been divided into six chapters. Chapter 1 is devoted to the introduction and motivation. Chapter 2 explains the RF heating model of AIMDs during MRI scans with its implementation on an AIMD inside a cylindrical human body model under the quasistatic assumption. Chapter 3 contains the materials and methods used for the testing of the analysis. Chapter 4 is devoted the obtained results whereas Chapter 5 goes into the discussions of the results. Finally, Chapter 6 includes the conclusions of the thesis with the future work.

In the appendix, additional information about the Fourier transform convention and the special integral identities used during the calculations are presented.

Chapter 2

Theory

2.1. Introduction

A typical active implantable medical device (AIMD) with a single lead is shown in Figure 1. In order to analyze the RF heating of these types of implants, a general configuration was developed. The length of the lead was shortened despite the fact that it is very long. Also, the lead was considered as curved rather than looped around itself.

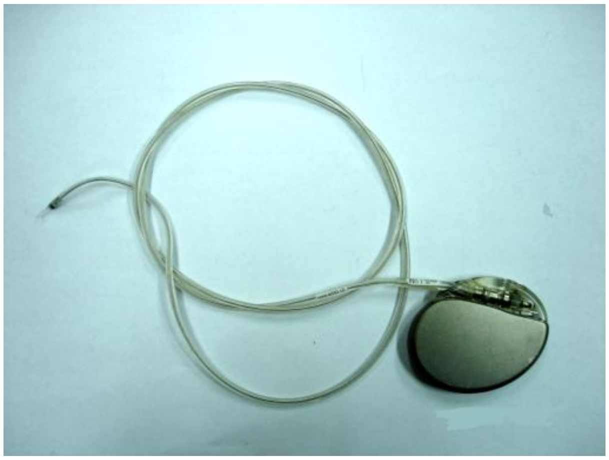

Figure 1. The photography of a typical active implantable medical device. The device shown in the figure is a pacemaker (Regency SC+ 2402L, Pacesetter, Switzerland).

In that chapter, first an early proposed RF heating model was explained. Also, the safety index of an AIMD was calculated based upon that model with underlined simplifying assumptions. The same derivations for the safety index were overviewed and simplified with a novel quadrature birdcage body coil model.

2.2. RF Heating Model

When a body undergoes an MRI examination, the body heats up due to the RF fields transmitted by the MRI scanner. The underlying mechanism behind the RF heating was modeled by Bottomley et al [19] and formulated what happens when there is an implant by Yeung et al [6]. This model was developed at 1.5 T for two cases; when there is an implant in the body and there is not an implant in the body. The detailed explanations are given in the following subsections.

2.2.1. RF Heating Model without Implants

RF heating of a body without an implant is the most common case. The body is exposed to the RF power of a transmitting body coil when there is no metallic implant in the body [20]. As shown in Figure 2, P is the time-averaged input power and determined by the applied RF pulse of the imaging sequence. This input power causes power deposition, characterized by specific absorption rate (SAR) and a function of position $\vec{r}$, in the body with respect to the electromagnetic properties of the tissue. Afterwards, this SAR distribution is converted into temperature distribution, which is a function of position $\vec{r}$ as well, depending on the thermal properties of the body [21].

Figure 2. Flow-chart model of RF heating in MRI when there is no implant in the body. This figure is copied from reference [21].

The SAR is calculated from the electric field distribution in the body according to the following equation:

$$SAR = \frac{\sigma}{\rho_t} |E|^2 \tag{1}$$

where σ is the electrical conductivity of the tissue , ρ_t is the mass density of the tissue, and E is the rms amplitude of the RF electric field transmitted by the body coil. This can be calculated by using Maxwell's equations.

The temperature distribution in the body can be calculated by the bioheat equation first proposed by Pennes [22].

$$\frac{dT(\overline{r},t)}{dt} = \alpha\,\nabla^2 T(\overline{r},t) - \frac{\alpha\,\rho_b\,c_b\,m}{c_t}\left(T(\overline{r},t) - T_b\right) + \frac{1}{c_t}\;SAR(\overline{r},t) + Q \qquad \textbf{(2)}$$

in which c_t and α are the heat capacity and thermal diffusivity of the tissue respectively, c_b, ρ_b and T_b in that order are the heat capacity, mass density and temperature of the perfusing blood, m is the volumetric flow rate of blood per unit mass, Q is the heat generated by normal chemical processes in the body, ∇ is the Laplacian operator, and $\overline{r}$ is the position vector. When it is assumed that metabolic heat generation keeps the core body temperature steady with the perfusing blood temperature [21], the Eq.(2) can be written as follows:

$$\frac{d\Delta T(\overline{r},t)}{dt} = \alpha\,\nabla^2\Delta T(\overline{r},t) - \alpha\,v^2\Delta T(\overline{r},t) + \frac{1}{c_t}SAR(\overline{r},t) \qquad \textbf{(3)}$$

where $\Delta T = T - T_b$ and *v,* defined as $v = \sqrt{\rho_b c_b m / \alpha c_t}$, is the lumped perfusion constant. Notice that with that assumption the effect of the thermoregulation constant, Q, is assumed to be zero.

Even if the analytical solution of Eq. (3) is not possible, in case of local heating, it is possible to achieve an approximate solution with the following simplifying assumptions. First, the thermal parameters are assumed to be constant around the point of interest over a small temperature range. Next, the local region is assumed to be small with respect to whole body and not near the surface of any boundary. With these assumptions, Green's function of the bioheat equation can be used to find the spatial temperature distribution [21] as the following equation:

$$\Delta T(\overline{r}) = SAR(\overline{r}) * G(\overline{r}) \qquad \textbf{(4)}$$

where ‘*’ denotes convolution and $G(\bar{r})$ is the Green’s function of the bioheat equation as a function of position vector.

Green’s function of the bioheat equation in the cylindrical (line source) and spherical (point source) coordinates for steady state are given respectively in Eq. (5) and Eq.(6).

$$G(R) = \frac{1}{2\pi\alpha c_t} K_0\left(vR\right) \quad \textbf{(5)}$$

$$G(r) = \frac{1}{\alpha c_t} \frac{e^{-vr}}{4\pi r} \quad \textbf{(6)}$$

where R is the distance from line source, r is the distance from point source, *v* is a lumped perfusion parameter, α is the diffusivity of the tissue, c_t is the heat capacity of the tissue, and K_0 is the modified Bessel function of the second kind and order zero.

The time-dependent Green’s function of the bioheat equation in cylindrical in and spherical in coordinates are given in [21].

2.2.2. RF Heating Model with Implants

RF heating of a body with an implant is a very complex case because of the coupling of the transmitting coil with the metallic implant [20]. When there is an implant in the body during an MRI procedure, the absorbed power (SAR) in the body is amplified around the implant. This amplification is quantified with SAR gain as shown in Figure3A. With current technology it is not possible to know the resultant amplified SAR, denoted SAR’ in Figure3A in the body. Yet, the deposited power when there is no implant in the body, that is SAR, can be estimated because the current MRI scanners are designed in a way that the applied power level is always lower than the patient safety limits. Therefore, it is reasonable to combine the raw SAR gain with the bioheat transfer into one unit, safety index [6], so that we can have a system with an estimated input, SAR, in order to be able find the resultant temperature distribution in the body as shown in Figure3B. This helps to ensure safety of patients with implants by setting limits on the applied SAR of the imaging pulse sequence.

Thus, the safety index expresses the temperature increase as a consequence of the existence of an implant in the body for each unit of peak applied *SAR* when there is no implant in the body.

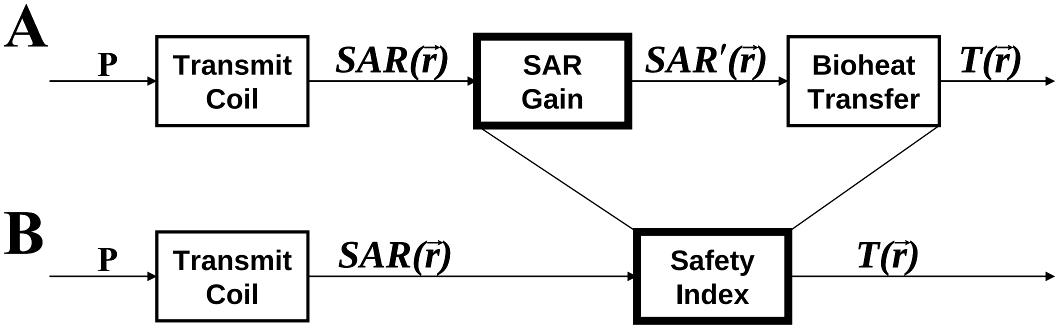

Figure 3. Flow-chart model of RF heating in MRI in case there exists an implant in the body. This figure is copied from reference [6].

2.3. Safety Index of Active Implants

With the proposed RF heating model for the existence of an implant in the body exposed to MRI-related RF fields, in that section, the safety index of active implants is obtained analytically by implementing each system in the RF heating model.

The analysis for the coupling of the transmit coil with a metallic implant in the body during an MRI examination is rather complicated despite the fact that it is straightforward for an electromagnetic solver software to analyze. Therefore, the theoretical analysis of the implant lead tip heating problem is not possible without some simplifying assumptions.

In order to make the first order approximation for the RF heating of an AIMD lead tip, the human body was assumed to be an infinitely long cylindrical object with uniform electromagnetic properties as in earlier studies [19, 23-25]. It was assumed to be lying coaxial with the transmit body coil. Besides, similar to these studies, the diameter of the body was assumed to be small compared to the wavelength.

On the other hand, considering the variety of AIMD configurations, the implant in Figure 1 was simplified for the analysis as shown in Figure 4. The common structure of an AIMD includes at least one insulated lead with a bare lead tip and a generator with a metallic case. Besides, the size of the implant including its leads was assumed to be significantly smaller than the wavelength; hence quasistatic RF fields can be used around the implant during the analysis.

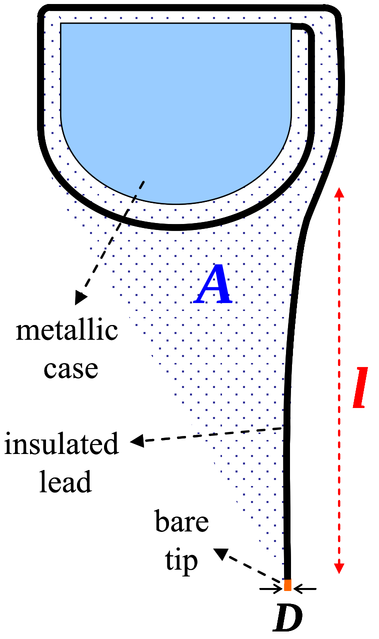

Figure 4. Model of an active implantable medical device. In this figure, D is the diameter of the tip; A is the area of the curvature; and l is the z-component of the distance between the metallic case and the electrode tip.

2.3.1. Calculation of SAR at the Implant Tip

The transmitted RF magnetic and electric fields of the body coil are coupled with the active implant in a way that a potential difference between the metallic case and the bare tip is induced. This gives rise to a current induction on the implant lead. This current is scattered from the bare tip to the tissue. Since tissue is a lossy medium, this scattered current amplifies the absorbed power already induced by the transmitted RF magnetic field in the body.

2.3.1.1. Calculation of Induced Current

There are two sources of voltage induction between the metallic case and the bare tip; the transmitted RF magnetic field and electric field. The resultant potential difference gives rise to a current induction at the lead tip of the implant depending on the impedance of the tip in a way that will be explained next. The equivalent circuit of an implant shown in Figure 5 illustrates the parameters affecting the current induction at the tip.

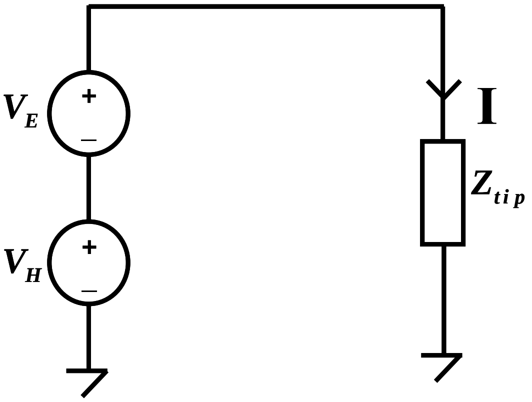

Figure 5. Equivalent circuit of the active implant model. V_E is the voltage source due to the coupling of the transmitted electric field with the straight part of the lead. V_H represents the voltage source because of the coupling of the transmitted magnetic field with the curvature of the lead. Z_{tip} is the impedance of the tip.

The first source comes from the coupling of the straight part of the lead with the incident electric field. It is calculated as follows:

$$V_e = \overline{E}_z(R) \cdot \overline{l} \quad \textbf{(7)}$$

where $E_z(R)$ is the transmitted electric field in longitudinal direction and varies only in the radial direction on the body, and l is the distance between the metallic case and the tip in z-direction. In most of the studies calculating the deposited power around a straight wire [6, 7]; the maximum coupling between the electric field and the straight wire was achieved when the electric field is incident parallel to the wire. In our case, the transmitted electric field was also parallel to the straight part of the lead for maximum coupling. Then, Eq.(7) is reduced to the following:

$$V_e = E_z(R)l \qquad \textbf{(8)}$$

Reilly and Diamant [26] used the same idea for the excitation of a nerve fiber by an external electric field to analyze the peripheral nerve stimulation.

On the other hand, the second source comes from the coupling of the curvature constructed by the lead with the RF magnetic field. This source of voltage induction can be calculated by Maxwell's Faraday's law of induction as shown below:

$$V_h = -j\omega\overline{B}_1.\overline{n}_A A \qquad \textbf{(9)}$$

in which A is the area of the loop and $\overline{n}_A$ is the normal vector of the loop and B_1 is the RF magnetic field. In fact, in many studies [3, 9-11, 27], it is mentioned that the effect of the existence of loops or curvature of leads can be calculated as shown in Eq. (9). Here, B_1 can be written in vector form depending on the left-hand rotation (this is the only one exciting the spins) convention as follows:

$$\overline{B}_1 = B_1\left(\hat{a}_x + j\hat{a}_y\right) \qquad \textbf{(10)}$$

For a general analysis of the implant structure, it was assumed that the normal of the loop makes an angle of β with x-axis as shown in Figure 6; therefore, it can be expressed in vector form as follows:

$$\overline{n}_A A = \hat{a}_x A\cos\beta + \hat{a}_y A\sin\beta \qquad \textbf{(11)}$$

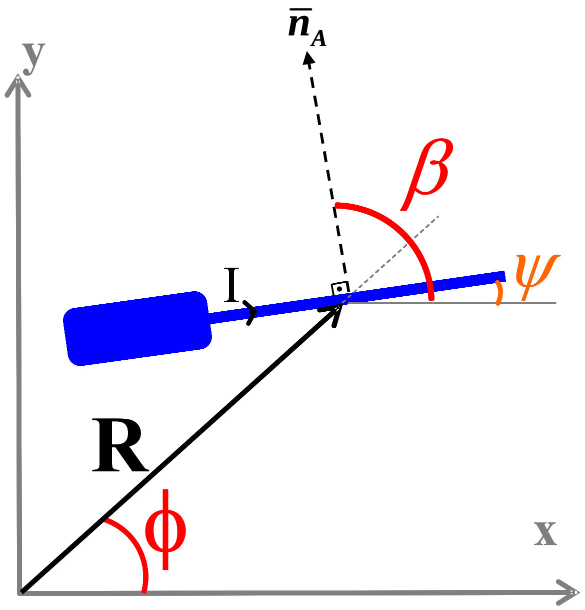

Figure 6. Axial view of the implant on the cylindrical human torso. I is the induced current flowing from the metallic case through the bare tip, that determines the direction of the normal vector $\overline{n}_A$ of curvature. Φ is the angle of the line connecting the center of the implant curvature to the origin of the cylindrical body. β is the angle between the normal of the loop and the x-axis. ψ is the angle that curvature of the implant makes with the x-axis.

Thus, the resultant induced voltage due to the curvature of the leads can be written as the following:

$$V_h = -j\omega B_1 A e^{j\beta} \tag{12}$$

As a result, the total induced voltage between metallic case and the tip can be written as follows:

$$V_{total} = E_z(R)l - j\omega B_1 A e^{j\beta} \tag{13}$$

We can write Eq. (13) in a more appropriate form as follows:

$$V_{total} = E_z(R)l + \omega B_1 A e^{j\psi} \tag{14}$$

in which ψ is defined as $\psi = \beta - \pi/2$ shown in Figure 6.

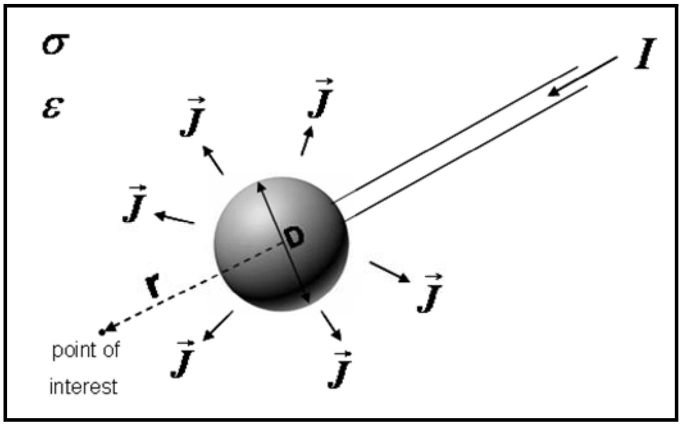

Figure 7. RF heating model of an insulated lead with bare tip, which is a very thin wire with spherical PEC tip. When current I is injected, current density J is distributed spherically symmetric to the tissue.

So as to find the induced current, call that current I, at the tip using the voltage difference between the bare tip and the metallic case, the impedance of the body to the tip should be calculated. For that purpose, the potential of the tip with respect to the lossy medium around it can be calculated by assuming a current I is induced at the tip. For simplicity, the metallic case and the tip were assumed as perfect electric conductor (PEC). While the insulated wire was assumed to be very thin, the tip was assumed to be a sphere with diameter D in order to take advantage of the spherical symmetry of the tip as shown in Figure 7. This assumption enabled to treat the bare tip as a point source, scattering current density around it. Thus, it became possible to use Green's function for a point source of the bioheat equation to calculate the heat transfer to the tissue. Assuming the bare tip as a PEC enabled the worst-case heating, because the small resistivity of the tip gives rise to maximum SAR amplification at the tip [28].

In a lossy medium, there are two types of current density in the system; conduction and displacement current densities as giving in Eq.(15). Due to the spherical symmetry, the current density is defined as in Eq. (16). Next, the scattered electric field can be found as in Eq. (17).

$$\overline{J} = \left(\sigma + j\omega\varepsilon\right)\overline{E} \quad \textbf{(15)}$$

$$J = \frac{I}{4\pi r^2} \tag{16}$$

$$E_r = \frac{\mathrm{I}}{(\sigma + j\omega\varepsilon)4\pi r^2} \tag{17}$$

Then, we can find the potential of the tip by integrating the scattered electric field with respect to the radial distance to the tip as shown below:

$$V_{tip} = -\int_{\infty}^{D/2} \overline{E} \cdot \overline{dr} \tag{18}$$

Thus, the potential of the tip becomes the following:

$$V_{tip} = \frac{\mathrm{I}}{2\pi(\sigma + j\omega\varepsilon)D} \tag{19}$$

Then, the impedance of the tip modeled as a spherical PEC in a dielectric medium can be formulated as follows:

$$Z_{tip} = \frac{1}{2\pi(\sigma + j\omega\varepsilon)D} \tag{20}$$

Notice that in Eq. (19) the potential of the tip decreases as the diameter of the tip increases. Therefore, we can consider the metallic case with a very large diameter so that its potential with respect to tip becomes negligible. Then, the voltage difference between the tip and the case can be approximated as the potential of the tip with respect to the dielectric medium around it. Then, the induced current at the tip can be found as the following:

$$\mathrm{I} = 2\pi(\sigma + j\omega\varepsilon)D\left(E_z(R)l + \omega B_1 A e^{j\psi}\right) \tag{21}$$

Using induced current on the lead, we can formulate the scattering electric field at the tip and consequently the amplified SAR at the tip. Thus, from Eq.(17), the induced electric field at the tip can be formulated in terms of the incident RF fields and the properties of the active implant as follows:

$$E_r(r) = \frac{D}{2r^2}\left(E_z(R)l + \omega B_1 A e^{j\psi}\right) \tag{22}$$

Next, the amplified deposited power at the tip of the implant can be calculated as a function of radial distance r as follows:

$$SAR'(r) = \frac{\sigma}{\rho_t}\left(\frac{D}{2r^2}\right)^2 \left|E_z(R)l + \omega B_1 A e^{j\psi}\right|^2 \quad \textbf{(23)}$$

Then, maximum amplified power can be written like this:

$$SAR'_{\max} = SAR'(r = D/2) = \frac{\sigma}{\rho_t}\left(\frac{2}{D}\right)^2 \left|E_z(R)l + \omega B_1 A e^{j\psi}\right|^2 \quad \textbf{(24)}$$

2.3.2. Calculation of Temperature Increase in the Tissue

With the known amplified SAR distribution, the temperature rise distribution can be calculated in terms of induced current I at the tip using Green’s function averaging technique [21] to take into account the bioheat transfer effects.

Notice that, in this study only the temperature increase due to the existence of the implant, in other words the amplified SAR (SAR’) at the tip will be calculated. Even if there is no implant in the body, body temperature increases due to the deposited power (baseline SAR) during an MRI procedure. However, this increase is kept limited by the MRI system, i.e. pulse sequences are adjusted in a way that the applied power is always lower than the safety limits. Therefore, the temperature rise due to the baseline SAR is not a safety concern and much lower compared to the one caused by the deposited power due to the existence of an implant (SAR’). SAR’ causes such a high temperature increase at the tissue that the tissue might burn. Thus, only the effect of scattered electric field on the temperature rise in the tissue was calculated by neglecting the one cause by the transmitted electric field.

From Eq. (23) , the amplified SAR at the tip can be formulated as follows:

$$SAR'(r) = \begin{cases} \dfrac{\sigma}{\rho_t}\left(\dfrac{D}{2}\right)^2 \left|E_z(R)l + \omega B_1 A e^{j\psi}\right|^2 \dfrac{1}{r^4}, & for\ r > \dfrac{D}{2} \\ 0, & for\ r < \dfrac{D}{2} \end{cases} \tag{25}$$

In steady-state, the Green's function of the tissue bioheat equation in spherical coordinates [21] for a point source is given as:

$$G(r) = \frac{1}{\alpha c_t}\frac{e^{-vr}}{4\pi r} \tag{26}$$

where c_t and α are the heat capacity and thermal diffusivity of the tissue respectively and v is a lumped perfusion constant and r is the distance from point source. Lumped perfusion constant is defined as $v = \sqrt{\rho_b c_b m / \alpha c_t}$, in which ρ_b and c_b are in that order the mass density and heat capacity of blood, and m is the volumetric flow rate of blood per unit mass of tissue [21].

Then, the amplified SAR can be convolved with the Green's function of the bioheat equation as it is given in Eq. (4). However, a different methodology suggested by Gao et al. [29] was followed for our calculations. That is, while calculating the resulting temperature distribution, the Fourier transform and its properties like convolution property given in Eq.(83) were used for simplicity rather than using convolution in computations directly. Thus, the Fourier transform of the amplified SAR was multiplied with the Fourier transform of the Green's function of the bioheat equation, and then their spherical inverse Fourier transform was taken to find the temperature increase.

The Fourier transform of spherically symmetric $SAR'(r)$ distribution was calculated using (81) in this way:

$$SAR'(q) = \frac{\sigma}{\rho_t}\left(\frac{D}{2}\right)^2 \left|E_z(R)l + \omega B_1 A e^{j\psi}\right|^2 \frac{4\pi}{q}\int_{\frac{D}{2}}^{\infty}\frac{\sin(qr)}{r^3}dr \tag{27}$$

The spherical Fourier transform (81) of Green's function can be found using the identity in Eq. (84) in this way:

$$G(q)=\frac{1}{\alpha c_t}\frac{1}{v^2+q^2} \tag{28}$$

Using (82) and (83),

$$\Delta T(r)=\frac{1}{(2\pi)^3}\int_0^\infty SAR'(q)G(q)\frac{\sin(qr)}{qr}4\pi q^2 dq \tag{29}$$

Yet, r in $SAR'(q)$ is not the same as r in $\Delta T(r)$, so the notation of $SAR'(q)$ was changed as r'.

$$\Delta T(r)=\frac{\sigma}{\rho_t}\left(\frac{D}{2}\right)^2 \left|E_z(R)l+\omega B_1 A e^{j\psi}\right|^2 \frac{1}{\alpha c_t}\frac{2}{\pi}\frac{1}{r}\int_0^\infty \left\{\int_{\frac{D}{2}}^\infty \frac{\sin(qr')}{r'^3}dr'\right\}\frac{1}{v^2+q^2}\sin(qr)dq \tag{30}$$

Here, a trick was made by changing the order of integrals.

$$\Delta T(r)=\frac{\sigma}{\rho_t}\left(\frac{D}{2}\right)^2 \left|E_z(R)l+\omega B_1 A e^{j\psi}\right|^2 \frac{1}{\alpha c_t}\frac{2}{\pi}\frac{1}{r}\int_{\frac{D}{2}}^\infty \frac{1}{r'^3}\left\{\int_0^\infty \frac{\sin(qr')\sin(qr)}{v^2+q^2}dq\right\}dr' \tag{31}$$

Using the trigonometric identity $2\sin(A)\sin(B)=\cos(A-B)-\cos(A+B)$

$$\Delta T(r)=\frac{\sigma}{\rho_t}\left(\frac{D}{2}\right)^2 \left|E_z(R)l+\omega B_1 A e^{j\psi}\right|^2 \frac{1}{\alpha c_t}\frac{2}{\pi}\frac{1}{r}\int_{\frac{D}{2}}^\infty \frac{1}{r'^3}\left\{\int_0^\infty \frac{\cos(q\,|\,r'-r\,|)-\cos(q(r'+r))}{2(v^2+q^2)}dq\right\}dr' \tag{32}$$

Using the integral identity in Eq. (85), the temperature increase can be written as follows:

$$\Delta T(r)=\frac{\sigma}{\rho_t}\left(\frac{D}{2}\right)^2 \left|E_z(R)l+\omega B_1 A e^{j\psi}\right|^2 \frac{1}{\alpha c_t}\frac{1}{2rv}\left\{\int_{\frac{D}{2}}^\infty \frac{e^{-|r'-r|v}}{r'^3}dr'-\int_{\frac{D}{2}}^\infty \frac{e^{-(r'+r)v}}{r'^3}dr'\right\} \tag{33}$$

After using the definition of the absolute value,

$$\Delta T(r)=\frac{\sigma}{\rho_t}\left(\frac{D}{2}\right)^2\left|E_z(R)l+\omega B_1 A e^{j\psi}\right|^2\frac{1}{\alpha c_t}\frac{1}{2rv}\left\{\int_{\frac{D}{2}}^{r}\frac{e^{(r'-r)v}}{r'^3}dr'+\int_{r}^{\infty}\frac{e^{-(r'-r)v}}{r'^3}dr'-\int_{\frac{D}{2}}^{\infty}\frac{e^{-(r'+r)v}}{r'^3}dr'\right\}$$

(34)

When $r=\frac{D}{2}$, maximum temperature increase on the tip was obtained. Then, the first integral in Eq. (34) disappears. After some arrangements in the arguments of exponentials by taking the common term D*v*/2 out of the parenthesis, the following equation can be observed:

$$\Delta T_{\max}=\frac{\sigma}{\rho_t}\left(\frac{D}{2}\right)^2\left|E_z(R)l+\omega B_1 A e^{j\psi}\right|^2\frac{1}{\alpha c_t}\frac{1}{Dv}\left\{\int_{\frac{D}{2}}^{\infty}\frac{e^{-(\frac{2r'}{D}-1)\frac{Dv}{2}}}{r'^3}dr'-\int_{\frac{D}{2}}^{\infty}\frac{e^{-(\frac{2r'}{D}+1)\frac{Dv}{2}}}{r'^3}dr'\right\}$$

(35)

By making a change of variable $\frac{2r'}{D}=r'' \Rightarrow dr'=\frac{D}{2}dr''$

$$\Delta T_{\max}=\frac{\sigma}{\rho_t}\left|E_z(R)l+\omega B_1 A e^{j\psi}\right|^2\frac{1}{2\alpha c_t}\frac{2}{Dv}\left\{\int_{1}^{\infty}\frac{e^{-(r''-1)\frac{Dv}{2}}}{r''^3}dr''-\int_{1}^{\infty}\frac{e^{-(r''+1)\frac{Dv}{2}}}{r''^3}dr''\right\}$$

(36)

Here, we call the numerical integral part of that expression *Perfusion Correction Factor* that is plotted in Figure 8.

$$f(Dv)=\frac{2}{Dv}\left\{\int_{1}^{\infty}\frac{e^{-(r''-1)\frac{Dv}{2}}}{r''^3}dr''-\int_{1}^{\infty}\frac{e^{-(r''+1)\frac{Dv}{2}}}{r''^3}dr''\right\}$$ **(37)**

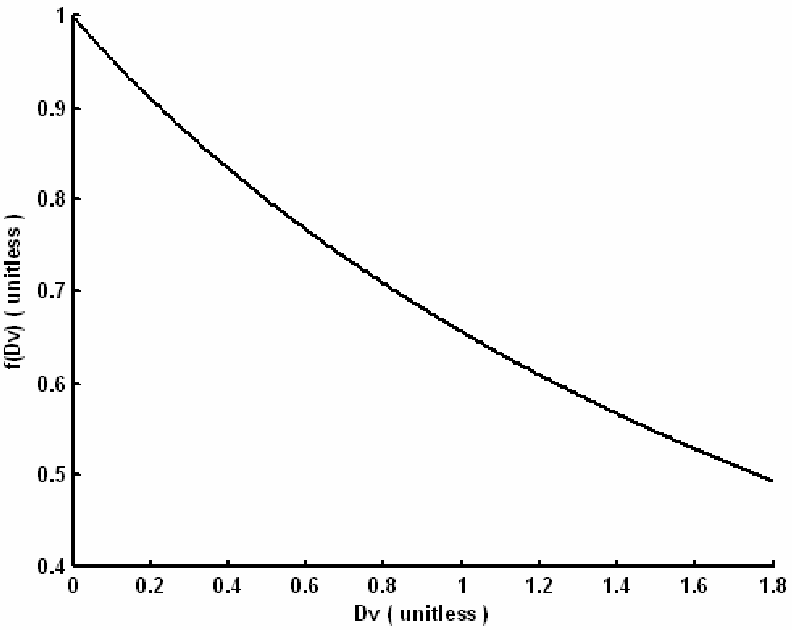

Figure 8. Perfusion correction factor. Although, it is a complicated function analytically, it has a simple appearance when plotted.

Then, maximum temperature rise can be written as the next:

$$\Delta T_{\max} = \frac{\sigma}{\rho_t} \left| E_z(R)l + \omega B_1 A e^{j\psi} \right|^2 \frac{f(Dv)}{2\alpha c_t} \quad \textbf{(38)}$$

From Eq. (21),

$$\Delta T_{max} = \frac{|I|^2}{8\pi^2} \frac{\sigma}{\left(\sigma^2 + \omega^2 \varepsilon^2\right)} \frac{1}{\alpha c_t \rho_t} \frac{1}{D^2} f(Dv) \quad \textbf{(39)}$$

That formulation illustrates the effect of induced current at the tip to the temperature increase in the tissue. Temperature rise can be limited by the induced current at the tip.

Finally, the safety index can be found as follows;

$$SI = \frac{\Delta T_{\max}}{SAR_{peak}} = \frac{\left| E_z(R)l + \omega B_1 A e^{j\psi} \right|^2}{\left| E_z(R_b) \right|^2} \frac{f(Dv)}{2\alpha c_t} \quad \textbf{(40)}$$

2.4. Modeling Fields inside the Body Coil

One of the main hardware components of an MRI scanner are RF coils. Their main function is to transmit the RF magnetic field B_1 homogeneously to the body in order to excite the spins. The spins are maintained in equilibrium by the static magnetic field B_0 before the RF magnetic field excites them to the plane perpendicular to B_0 field. Then, an MR signal is obtained. The reception of this MR signal is performed by RF coils as well.

However, the design of an RF coil with homogeneous transmission is a very challenging task and another research area. It is desirable to produce a high signal-to-noise ratio (SNR) in MRI systems to obtain a better spatial resolution in the images. SNR is defines as the B_1 field produced per unit coil current and tissue losses. This is succeeded with high static field intensity. As the intensity of B_0 field increases, the frequency of the B_1 field also increases. Considering the wavelength of the B_1 field, at higher frequencies the portion of the biological body to be imaged can be comparably large or even larger than the wavelength. Thus, this yields a stronger interaction between the biological tissues and the electromagnetic field. This interaction not only corrupt the B_1 field homogeneity; consequently causing low quality images, but also causes more power deposition in the body resulting safety problems for the MRI systems. Concerning the safety issues, the high frequency and increased B_1 field homogeneity introduces much intense electric field and accordingly eddy currents. These currents give rise to increased specific absorption rate (SAR) which is the primary source of temperature increase in the tissue [30].

Ever since they were introduced in 1985 [31], birdcage coils have been extensively used as a body coil in MR scanners due to their high RF field, B_1, homogeneity and high SNR over a large volume inside the coil. Homogeneity of RF field inside a birdcage coil is proportional to the number of excitations constructed at the corresponding legs of the coil. With birdcage coils, two types of excitation are possible; linear excitation and quadratic excitation. Linear excitation gives rise to a linearly polarized B_1 field when it is fed at a single point while quadratic excitation produces a circularly polarized B_1 field when it is fed at two points perpendicular to each other with a phase difference of 90° [32]. Quadrature birdcage coils have more advantages than linear ones in terms of the excitation power with 50% reduction and SNR with $\sqrt{2}$ times amplification [23]. Therefore, quadrature birdcage coils are widely used in the current MRI systems.

The safety problem of electromagnetic interaction with the human body during MRI scans has been studied comprehensively for many years. Earlier works used an approximate model of human body, an infinitely long homogeneous cylindrical body [19, 23-25], and the resultant analytical solution of the problem showed that as the frequency of B_1 field increases, the homogeneity of B_1 field decrease while SAR in the object increases as well. With the advance of computer processor speed and electromagnetic simulators, it becomes possible to solve Maxwell's equations accurately on the two dimensional (2D) [32] and three dimensional (3D) [30, 33, 34] models of human body. Despite the fact that these numerical solutions provide a beneficial insight of the safety problem of MRI (especially at high frequencies between 64 MHz and 300 MHz) and validate the results of analytical solutions, they are expressed in complicated expressions, but make sense with their simulations.

Since the purpose in that study is to develop an analytical study to derive a simple and easy to use safety index formula, an analytical relationship between the transmitted electric field and RF magnetic field is needed. Because of this, we analytically calculated the RF magnetic field, B_1, over an approximate human body model, an infinitely long cylinder with homogeneous electrical properties, inside a quadrature birdcage coil. Since most of the MRI systems use circularly polarized quadrature birdcage body coil due to its high field homogeneity, we developed this model for quadrature birdcage body coil to generate a homogeneous transverse RF magnetic field in the human subject.

In order to analyze the safety index of an active implant that is absolutely independent of the MRI system used, phase distribution of the transmitter must be carefully adjusted so that worst-case tip heating is guaranteed [35]. Thus, the quasistatic MRI fields for the analysis were assumed, so that the phase of the fields varies slowly on the implant that is small in comparison with the wavelength; therefore, constructive addition of fields at the tip was enabled for maximum heating. This phase distribution is even worse than the worst case heating distribution mentioned in [35]. As a result, plane waves can be used as a source of excitation. Then, assuming a homogeneous RF magnetic field, B_1, inside the body coil, the incident electric field on the implant with a slowly varying linear magnitude and worst-case phase distribution can be derived as a function of position.

For circularly polarized plane waves, at least two linearly polarized plane waves with a 90° phase difference are needed. As the simplest approximation for the birdcage coil, four plane waves were used considering the circular geometry of the coil with equal magnitudes and appropriate phases to achieve circular polarization. In fact, infinitely many excitations would be ideally more accurate for the modeling of a birdcage coil. Yet, for the ease of calculation, four plane waves were enough for the purpose.

As a background, it should be kept in mind the following constitutive relation;

$$B_1 = \mu H_1 \tag{41}$$

in which B_1 is the magnetic flux density and H_1 is the magnetic field intensity.

While the main magnetic field, B_0, is in the z-direction, the RF magnetic field, B_1, has only transverse components and they can be written as a sum of the left and right hand circularly polarized rotating field components as in the Eq. (42).

$$\bar{H}_1 = \hat{a}_x H_x + \hat{a}_y H_y = \hat{a}_- H_- + \hat{a}_+ H_+ \tag{42}$$

where $\hat{a}_-$ is the left-hand sense (clockwise) rotation axis and $\hat{a}_+$ is the right-hand sense (counter-clockwise) rotation axis, which are defined as follows:

$$\hat{a}_- = \hat{a}_x + j\hat{a}_y \quad \textit{and} \quad H_- = (H_x - jH_y)/2 \tag{43}$$

$$\hat{a}_+ = \hat{a}_x - j\hat{a}_y \quad \textit{and} \quad H_+ = (H_x + jH_y)/2 \tag{44}$$

in which we can estimate the magnitude of magnetic field intensity, H_1, from the imaging parameters, i.e. flip angle, pulse sequence, TR.

As a rotating frame of reference, left-hand sense rotating frame was assumed because it is the only component that produces a torque on the magnetization of hydrogen spins at the larmor frequency, while the other component has no effect.

Consequently, the formulation was based on the mentioned assumptions and references for the construction of plane waves in Figure.

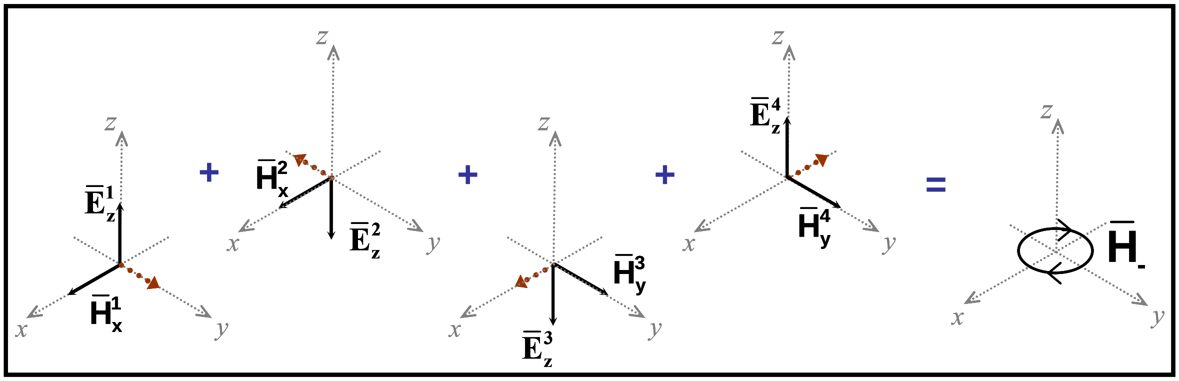

Figure 9. Representation of quadrature birdcage coil with plane waves.

We can write the wave equations of plane waves at the center of the body with the same amplitude considering their propagation directions as follows:

$$\bar{H}_x^1 = \hat{a}_x \frac{H_-}{2} e^{-jk_c y} \quad \textbf{(45)}$$

$$\bar{H}_x^2 = \hat{a}_x \frac{H_-}{2} e^{jk_c y} \quad \textbf{(46)}$$

$$\bar{H}_y^3 = j\,\hat{a}_y \frac{H_-}{2} e^{-jk_c x} \quad \textbf{(47)}$$

$$\bar{H}_y^4 = j\,\hat{a}_y \frac{H_-}{2} e^{jk_c x} \quad \textbf{(48)}$$

Then, the total magnetic field intensity gives the following:

$$\bar{H}_1 = H_- \left(\hat{a}_x \cos\left(k_c y\right) + j\hat{a}_y \cos\left(k_c x\right)\right) \quad \textbf{(49)}$$

where H_- is the magnetic field intensity, $\hat{a}_x$ and $\hat{a}_y$ are the unit vectors, x and y are the distance variables on the corresponding cartesian coordinates, and j is the complex number, $j = \sqrt{-1}$ a and k_c is the complex wavenumber. For circular polarization, $H_- = H_{10}(1-j)/2$. The complex wave number is calculated [36] as $k_c = \sqrt{\omega^2 \mu\varepsilon - j\omega\mu\sigma}$,in which ω is the angular frequency, and μ, ε and σ are respectively the magnetic permeability, electrical permittivity and conductivity of the tissue. Notice that for small k_c and distance from the center of the cylindrical human body, Eq. (49), gives the next:

$$\bar{H}_1 = H_-\left(\hat{a}_x + j\hat{a}_y\right) \quad \textbf{(50)}$$

that is consistent with the definition of left hand circularly polarized magnetic field intensity.

With that excitation scheme, left hand circularly polarized magnetic field was ensured only at the center of the body.

Next, from Maxwell's Ampere's law in time-harmonic form, that is $\nabla \times \overline{H} = (\sigma + j\omega\varepsilon)\overline{E}$, the following expression for the induced electric field on the longitudinal axis is obtained:

$$\overline{E}_z = \hat{a}_z \frac{H_- k_c}{(\sigma + j\omega\varepsilon)} \{\sin(k_c y) - j\sin(k_c x)\} \qquad \textbf{(51)}$$

For small $k_c x$ and $k_c y$, the following approximation can be made; $\sin(k_c x) \approx k_c x$ and $\sin(k_c y) \approx k_c y$. This yields the following:

$$\overline{E}_z = -\hat{a}_z \, \mu H_- \, \omega (x + jy) \qquad \textbf{(52)}$$

Eq. (52) can be written in cylindrical coordinates considering the geometry of the body inside the body coil. Then, the final form of the induced electric field was obtained in the body as a function of radial distance R (m) from the center of the human body and the cylindrical angular coordinate ϕ (rad) as follows:

$$E_z(R) = -\omega \mu H_- \, \mathrm{R} \, \mathrm{e}^{j\phi} \qquad \textbf{(53)}$$

It might be beneficial to express H_- in Eq. (43) in cylindrical coordinates for the purpose of comparison. While the unit vector with magnitude $\sqrt{2}$ is defined as in Eq. (54) , the left-hand rotating frame vector can be expressed as in Eq. (55).

$$\hat{a}_- = (\hat{a}_\rho + j\hat{a}_\phi) e^{j\phi} \qquad \textbf{(54)}$$

$$H_- = (H_\rho - jH_\phi)/2 \qquad \textbf{(55)}$$

Then, Eq. (53) is reduced to the following;

$$E_z(R) = -\omega \mu H_- \, \mathrm{R} \qquad \textbf{(56)}$$

The same relationship between the incident electric field and the RF magnetic field can be obtained by solving the cylindrical wave expressions given in [37] for modes $m = 1$ and $n = 0$ for a large wavelength.

Using the relationship in Eq.(53), we can obtain more compact formulations for the induced current and SAR amplification at the tip, and safety index of active implantable medical devices.

2.4.1. Safety Index of Active Implants using Body Coil Field Model

The induced voltage between the tip and the metallic case can be written in terms of the induced electric field using Eq. (53) in Eq. (14).

$$V_{total} = \left(l + \frac{A}{R} e^{j\theta} \right) E_z(R) \tag{57}$$

in which $\theta = \pi + \psi - \phi = \beta - \phi + \pi / 2$ as shown in Figure 10.

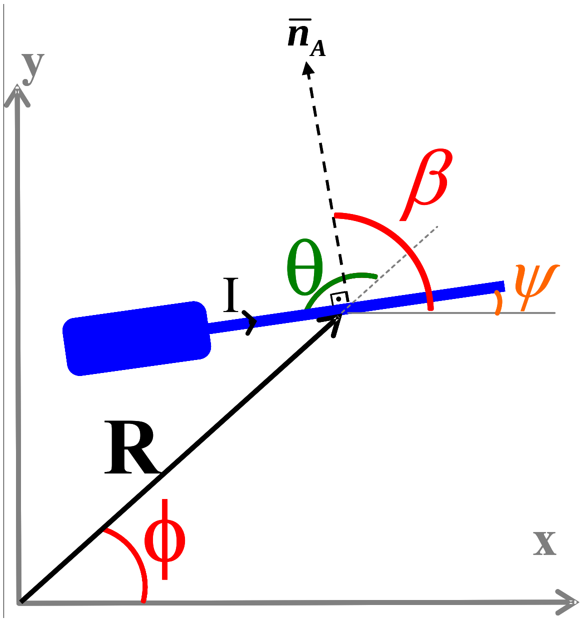

Figure 10. Axial view of the implant on the cylindrical human torso (see Figure 6 for a detailed description). θ is the angle that curvature of the implant makes with the radial axis connecting the center of the curvature with the center of the cylindrical object.

Yet, it is better to write induced voltage in terms of the maximum induced electric field in the body by taking advantage of Eq. (58) to avoid the misunderstanding that at the center it will be induced infinitely large.

$$E_z(R) = \frac{R}{R_b} E_z(R_b) \tag{58}$$

where R_b is the radius of the cylindrical body. Considering that induced electric field is a linear function of radial distance in the body, maximum electric field is induced at the periphery of the body. Then Eq. (57) is reduced to the following;

$$V_{total} = \left(Rl + Ae^{j\theta}\right)\frac{E_z(R_b)}{R_b} \quad \textbf{(59)}$$

Then the induced current at the tip in Eq. (21) was reduced to the next equation;

$$\mathrm{I} = 2\pi(\sigma + j\omega\varepsilon)\frac{D}{R_b}\left(Rl + Ae^{j\theta}\right)E_z(R_b) \quad \textbf{(60)}$$

Next, the amplified SAR at the tip becomes;

$$SAR'(r) = \frac{\sigma}{\rho_t}\,|\,E_z(R_b)\,|^2\left|Rl + Ae^{j\theta}\right|^2\left(\frac{D}{2R_b r^2}\right)^2 \quad \textbf{(61)}$$

Notice that it can be written in terms of the peak SAR without the implant in place as follows:

$$SAR'(r) = SAR_{peak}\left|Rl + Ae^{j\theta}\right|^2\left(\frac{D}{2R_b r^2}\right)^2 \quad \textbf{(62)}$$

Then maximum amplified power is the one obtained at the closest point to the tip that is $r = D/2$.

$$SAR'_{\max} = SAR_{\text{peak}}\left|Rl + Ae^{j\theta}\right|^2\left(\frac{2}{DR_b}\right)^2 \quad \textbf{(63)}$$

Thus, from the information given we can formulate SAR gain as follows;

$$SAR\,gain = \frac{SAR'_{\max}}{SAR_{\text{peak}}} = \left|Rl + Ae^{j\theta}\right|^2\left(\frac{2}{DR_b}\right)^2 \quad \textbf{(64)}$$

In other words, it can be defined as;

$$SAR\,gain = \frac{SAR'_{\max}}{SAR_{\text{peak}}} = \frac{|\,E(D/2)\,|^2}{|\,E_z(R_b)\,|^2} \quad \textbf{(65)}$$

Thus, SAR gain is the ratio of the amplified SAR at the tip of the implant, denoted as maximum SAR’, to the maximum SAR in the body without the implant in place.

Consequently, using Eq. (62) temperature increase can be calculated as seen below:

$$\Delta T_{\max} = \frac{SAR_{\text{peak}}}{R_b^2} \left| Rl + Ae^{j\theta} \right|^2 \frac{1}{2\alpha c_t} f(Dv) \tag{66}$$

Finally, safety index can be defined in terms of the peak SAR in the body when there is no implant in the body as shown in the next line;

$$SI = \frac{\Delta T_{\max}}{SAR_{\text{peak}}} = \frac{1}{2\alpha c_t R_b^2} \left| Rl + Ae^{j\theta} \right|^2 f(Dv) \tag{67}$$

Chapter 3

Materials and Methods

3.1 Introduction

After developing an analytical solution of the RF heating of an AIMD during MRI exams and ending up with related formulas to identify the parameters of the problem, the simulations of the model was performed in a computer environment to debug the derived formulas and check their accuracy. Then, we tried to make a phantom to mimic a homogeneous cylindrical human torso in order to validate our quadrature birdcage model and measure the safety index.

3.2 MATLAB Simulations

Despite the fact that the derivations were simplified as much as possible, there left some integrals that could not be solved analytically. *Perfusion Correction Factor* is the one that is a combination of two complicated integrals. Therefore, we tried to analyze this part numerically by MATLAB 6.5 (Matworks Inc.).

Besides, the additional calculations for the evaluation of the formulas for comparing them with electromagnetic solver results were done in MATLAB. Also the data fit for the experimental data was done with MATLAB's curve fitting tool. The first order polynomial fit of the data was performed with linear least squares method.

3.3 Electromagnetic (EM) Simulations

In our simulations, a commercial method of moments solver software called FEKO (EM Software & Systems; Stellenbosch, South Africa) was used.

During the simulations the electrical conductivity and the relative electrical permittivity of the medium was respectively assigned as 0.2 S/m and 66. In spite of the fact that these values are not representative of the average values for human tissues [38], it was preferred to use these values due to the fact that they were very practical during the preparation of the experiment setup.

3.3.1 Simulation of Quadrature Birdcage Coil Model

In this part, four plane waves were used to obtain a left-hand circularly polarized RF magnetic field at the center of the cylindrical human torso for the excitation as proposed in the theory part. As a result, the RF magnetic field and the incident electric field at the radial points were simulated to verify the formula in Eq. (56). Later, these results were used in the following analytical calculations of the induced current to compare with the results obtained from the EM simulations.

3.3.2 Simulation of Induced Current at the Tip

In that part, a simplified version of an AIMD was placed inside the quadrature birdcage coil model and measured the induced current at the tip.

The case of the implant was simply assumed as a rectangular prism with dimensions of the 5cmx5cmx0.8cm for the ease of theoretical calculations. The tip was modeled as a sphere as it was assumed during the theoretical analysis. While the case and the spherical tip was defined as a PEC, the wire connecting them was insulated with 0.35mm Teflon ($\sigma = 0$, $\varepsilon_r = 2.3$, $\mu_r = 1$).

First, only the effect of the wire length, *l*, between the tip and the case was simulated by assuming there is no curvature as shown in Figure 11 and then in that configuration the effect of the radial distance of the implant to the center of the body was observed.

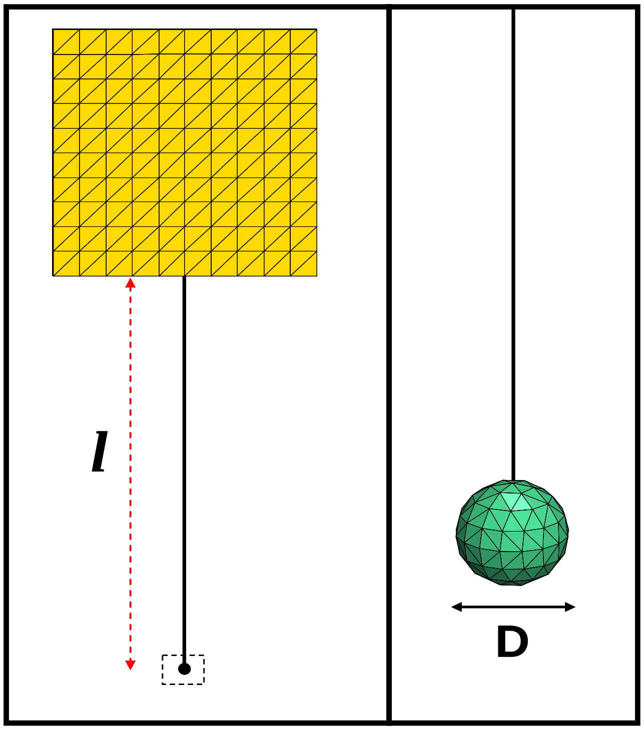

Figure 11. Left Panel: The simplified configuration of the implant without curvature of the lead in EM simulations. The implant was excited by quadrature birdcage coil model. **Right Panel:** The spherical tip of the implant is zoomed in.

Next, the effect of the curvature of the lead was simulated without any wire length between the case and the tip as shown in Figure 12. In that configuration, the effect of the area of the curvature was observed while the location of the curvature center was fixed, and for a constant area of the curvature, the effect of the loop center location was analyzed.

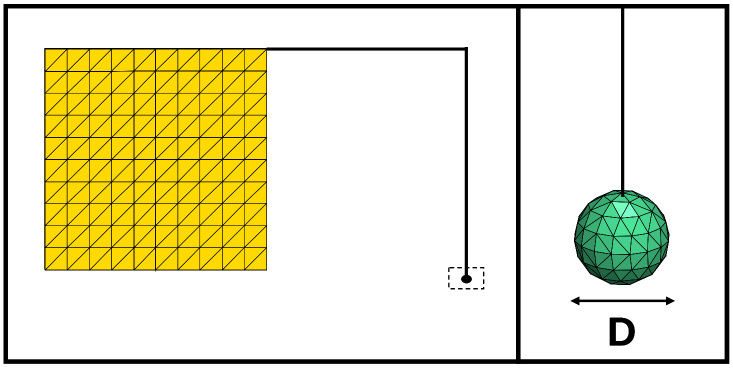

Figure 12. Left Panel: The simplified configuration of the implant with only loop in EM simulations. The implant was excited by quadrature birdcage coil model. **Right Panel:** The spherical tip of the implant is zoomed in.

3.3.3 Simulation of Gel Phantom

During the theoretical analysis, the human body was modeled as an infinitely long cylinder. Since in the experiments a cylindrical phantom container with a limited length can be used, it was critical to determine at which points the measurements should be taken so as to get valuable data from phantom experiments. Therefore, as a preparation for the gel experiments, the phantom inside the quadrature birdcage coil model was simulated as shown in Figure 13. The dimension of the phantom was the same as the one used in the experiments.

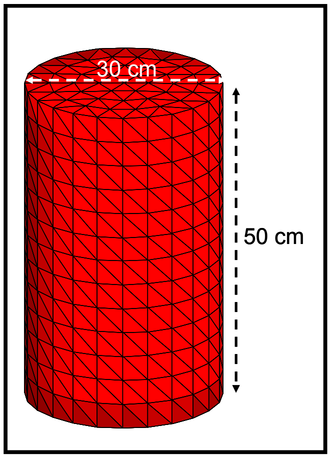

Figure 13. Simulation of phantom inside the quadratue birdcage coil model in the EM simulation.

3.4 Phantom Experiments

In order to perform phantom experiments, a cylindrical phantom container with 30 cm diameter and 50 cm length was constructed. Since the cylindrical phantom container has a very large volume, use of jello (fruit-flavored dessert made from gelatin powder) rather than polyacrylamide gel was preferred. This material is very cheap compared to polyacrylamide gel and commercially available in the stores. In spite of the fact that there are many companies producing jello, a brand called Dr. Oetker was used in the experiments. The main idea is to use a material that is viscous enough to prevent convection inside the phantom for the worst-case (perfusionless case) phantom that mimics the thermal and electrical properties of human tissue. The jello used in the experiment could provide enough viscosity when it was prepared using much more than the given recipe.

The gel phantom was constructed in a way that at the bottom, jello was poured until the required height (that will be understood in the simulation of gel phantom). After jello became viscous enough, NaCl solution was added on it as shown in Figure 15.

To provide electrical conductivity, a certain amount of sodium chloride (NaCl) was added to the jello. To decide how much NaCl was needed, the input impedance of a lossy transmission line was measured with the network analyzer (Model 8753D; Hewlett Packard, Palo Alto, CA). The lossy transmission line was imitated with a cylindrical parallel plate copper conductor inside which jello was poured to create a dielectric medium (for detailed explanation refer to [39]). To test the variability of the measurement, three setups that are totally the same were prepared. Since the more NaCl, the more difficult viscous jello to get, a small amount of NaCl was preferred to use. A 2.6 gr of NaCl was decided to be added to the gel made of 600 gr jello and 1lt of water. Consequently, an electrical conductivity of approximately 0.2 S/m and relative electrical permittivity of approximately 66 were achieved as an average of the measurements done with these three setups shown in Table 1. In order to obtain the same electrical properties inside NaCl solution, 1.3 gr NaCl was added to the 1lt of water.

Table 1. The conductivity and electrical permittivity measurements of prepared gel.

	σ (S/m)	**ε_r**
S_1	0.1794	63
S_2	0.2018	72
S_3	0.1839	64
S_{mean}	0.1884	66.3

To compare the measured electrical properties with human data, dielectric properties of heart (for pacemakers), brain (for deep brain stimulators) and blood are given in Table 2. Notice that the measured dielectric properties of jello are lower than the human data for the specified tissues. It is possible to arrange them by adjusting the amount of NaCl in the jello. Yet, the disadvantage of using jello is that it becomes more difficult to make it viscous as the NaCl content in it increases. The main idea for the experiments is to know the dielectric properties of the jello so that the derived formulations can be checked.

Table 2. Dielectric properties of the human heart, brain and blood [38].

Tissue	**σ (S/m)**	**ε_r**
Heart	0.68	106.65
Brain	0.4	82.75
Blood	1.21	86.54

Using the thermal property measurement kit (KD2 Pro, Decagon Devices Inc.) the thermal properties of the jello was measured as follows; heat capacity c_t

= 3965 J/kg/ºC, thermal conductivity k = 0.543 W/m/ ºC, diffusivity α = 0.137 mm^2/sec. The measured values are in the range of human thermal properties. To show this, the thermal properties of the heart, brain and blood were obtained after a literature survey in Table 3. Notice that once heat capacity, thermal conductivity and mass density is known, the diffusivity can be calculated by $\alpha = k/\left(\rho_t c_t\right)$.

Table 3. Thermal properties of human heart, brain and blood.

Tissue	ρ_t (kg/m^3)	k (W/m/ºC)	c_t (J/kg/ºC)	Reference
Heart	1030 -1060	0.54 - 0.59	3700 - 3900	[40, 41]
Brain	1027.4 -1050	0.16 - 0.57	3600 - 3800	[40-44]
Blood	1055 - 1060	0.49 – 0.56	3600 - 3900	[40, 42-44]

In order to measure, the temperature increase inside the phantom, fiber optic temperature probes (Neoptix, Quebec, Canada) were used.

To validate the electric field distribution inside the cylindrical phantom without the implant is in place, a phantom experiment was conducted in a GE Signa MR scanner. The Fast SPGR pulse sequence was used with pulse repetition time TR = 6 msec with a transmit gain TG_0 = 125 for a flip angle of α_0 = 90° after an autoprescan. Transmit gain (TG) is not a generic parameter for all scanners, but it is used in a GE scanner. It determines the RF power emitted by the transmit coil and quantified in tenths of decibels (dB). TG must be adjusted for scanning of each object, since deposited SAR, which is proportional to the square of the flip angle, depends on the size of the object. Therefore, before each scan, an autoprescan must be performed to calibrate TG by determining the amount of the deposited power to produce a 90º flip angle [45]. After calibrating the TG of the scanner with an autoprescan, the transmit gain was increased manually to TG = 190 in order to observe a detectable temperature increase inside the gel. Otherwise, even the scan time (approximately 23 minutes) would not be enough to observe any temperature increase inside the gel, because there was no implant inside the gel. Then, the corresponding flip angle was calculated as follows:

$$\alpha = \alpha_0 \cdot 10^{[(TG - TG_0)/200]} \quad \textbf{(68)}$$

From Eq.(68), the corresponding flip angle was calculated as α = 190.214° which is equal to 1.1π radians. With that knowledge, H_{1rms} should be calculated. The applied RF magnetic field in the repetition time (TR) is defined as follows:

$$H_1(t) = H_1 \int_0^{TR} e(t) \quad \textbf{(69)}$$

in which H_1 and $e(\tau)$ are the amplitude and the envelope of the RF magnetic field. Then the flip angle can be calculated as in the next expression:

$$\alpha = \gamma \mu H_1(t) \quad \textbf{(70)}$$

where γ is the gyromagnetic ratio (2π 42.576 MHz/T) and μ is the magnetic permeability. Next, H_{1rms} can be calculated as follows:

$$H_{1_{rms}} = \frac{\alpha}{\gamma \mu \int_0^{TR} e(\tau) d\tau} \sqrt{\frac{1}{TR} \int_0^{TR} e^2(\tau) d\tau} \quad \textbf{(71)}$$

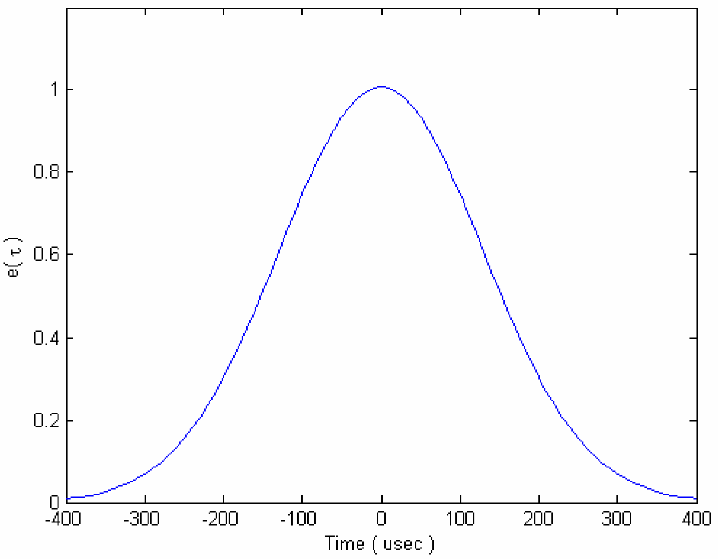

Figure 14. The envelope of the RF magnetic field.

The envelope of the RF magnetic field was measured with the oscilloscope as shown in Figure 14, so the required integrals in Eq.(71) in this way:

$$\int_0^{TR} e(\tau)d\tau = 325.6\times10^{-6} \tag{72}$$

$$\int_0^{TR} e^2(\tau)d\tau = 231.9\times10^{-6} \tag{73}$$

Then, the theoretical transmitted electric field was calculated using Eq.(56) and the resultant SAR was found using Eq. (1).

On the other hand, the consequent SAR obtained from the experiment can be calculated by calorimetry as follows:

$$SAR = c_t \frac{\Delta T}{\Delta t} \tag{74}$$

in which ΔT/Δt is the initial slope of the temperature rise obtained in the experiment.

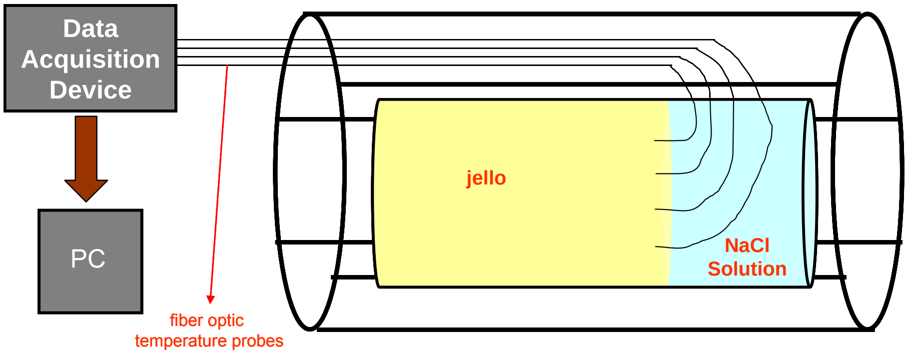

Figure 15. The experimental setup for the phantom experiment.

The probes were located as shown in Figure 16.The height of the gel was 24 cm inside the phantom container and the rest of it was filled with NaCl solution. The probes were 4 cm deeper from the surface of the gel. Thus, the measurements at the height of 20 cm were taken. Six experiments were conducted to measure the temperature increase at the marked locations. The resultant SAR was calculated using Eq.(74). The theoretical SAR values were calculated using Eq. (1) with the known transmitted electric field distribution of the used MRI sequence using Eq.(71) and Eq. (53).

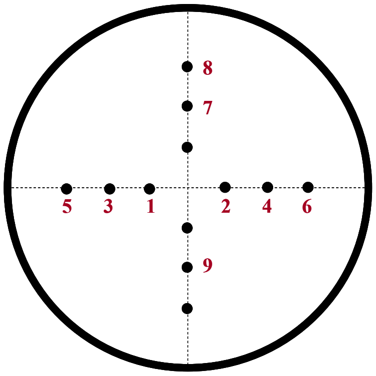

Figure 16. Axial view of the phantom container with probes inserted into the gel. The probes 1 and 2 are located 3 cm away from the center of the phantom. The probes 2, 4, 7, and 9 are placed 6 cm away while probes 5 and 6 are located 9 cm away from the center of the phantom.

Chapter 4

Results

4.1 Matlab Results

Even if *Perfusion Correction Factor* in Eq.(37) seems like a complicated function analytically, it is simply a decaying function of unitless quantity Dv as shown in Figure 8. It is equal to 1 for the worst-case RF heating condition which is perfusionless case. All calculations can be done assuming that worst-case condition and then the results can be normalized with respect to the desired perfusion value if needed.

4.2 Simulation Results

4.2.1 Results of Quadrature Birdcage Coil Model

The simulation results obtained at 63.8 Hz is shown in Figure 17 for the RF magnetic field and Figure 18 for the RF electric field. It is seen that at that frequency, the RF magnetic field is totally uniform inside the quadrature birdcage coil at all data points with respect to the radial distance away from the center of the cylindrical human torso model.

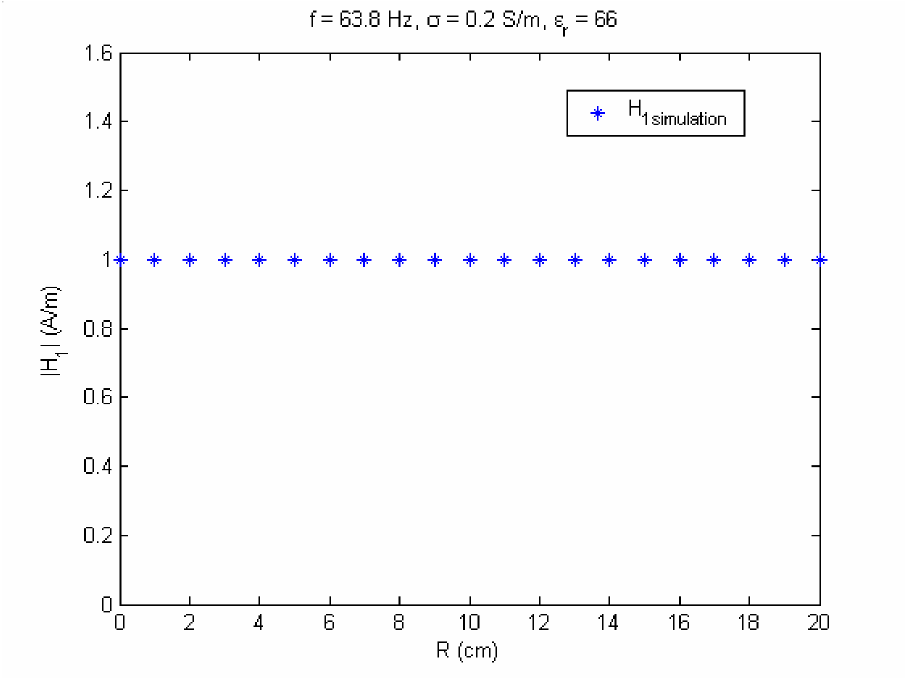

Figure 17. The RF magnetic field at 63.8 Hz observed from the quadrature birdcage coil model.

Yet, before using the magnetic field data for calculating the incident electric field inside the body it should be kept in mind that the magnetic field results of EM simulation should be normalized with $\sqrt{2}$. The reason for that is the rotating frame convention assumed at the beginning of the derivations. The convention accepted is different than the one used in EM simulation. In simulation, the magnitude of the rotating frame unit vector is equal to 1 as can be seen in Eq.(75) and consequently the RF magnetic field can be calculated as in Eq.(76). Whereas, the RF magnetic field in the derivations can be calculated as in Eq.(55) since the unit vector convention yields a vector with magnitude $\sqrt{2}$.

$$\hat{a}_{-}^{FEKO} = \left(\hat{a}_x + j\hat{a}_y\right)/\sqrt{2} \qquad \textbf{(75)}$$

$$H_{-}^{FEKO} = (H_x - jH_y)/\sqrt{2} \qquad \textbf{(76)}$$

As a result, since the quasistatic assumption was assumed at the beginning of the analysis, perfectly matching results with the EM simulation were obtained from the theoretical formulation.

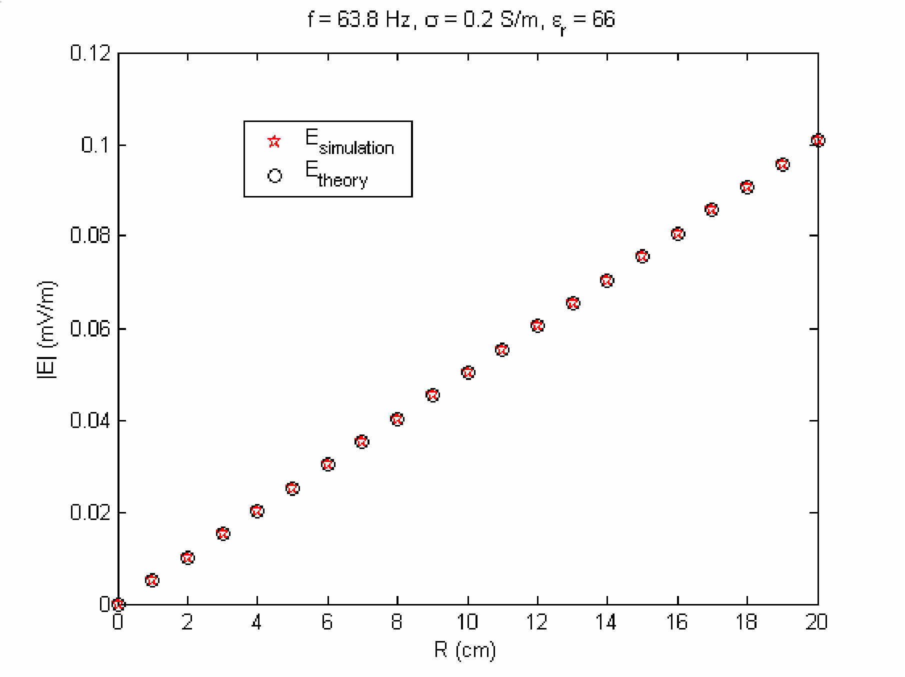

Figure 18. The transmitted RF electric field at 63.8 Hz observed from the quadrature birdcage coil model.

As much as the phases of the fields are concerned, it is seen in the EM simulation that the φ component of the magnetic field leads 90° the ρ component, while the phase of the magnetic field is equal to the one of ρ component for all radial distances from the center of the body. The phase of the transmitted electric field leads 180° the one of the RF magnetic field as expected from Eq. (56) again for all data points.

Considering the results obtained at 63.8 MHz, the plots of the RF magnetic field and the incident electric field are in that order shown in Figure 19 and Figure 20.

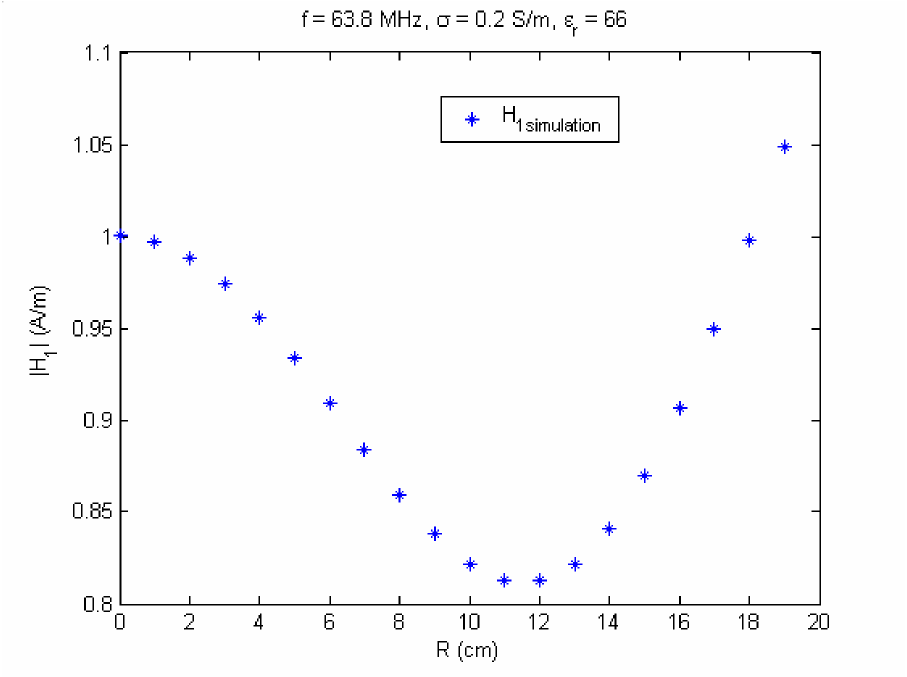

Figure 19. The RF magnetic field at 63.8 MHz observed from the quadrature birdcage coil model.

Contrary to the RF magnetic field obtained at 63.8 Hz, the RF magnetic field at 63.8 MHz is not uniform inside the body as shown in Figure 19 Therefore, in order to calculate the transmitted electric field inside the body only the magnetic field value obtained at the center of the body was used. Because, according to the quasistatic assumption, transmitted magnetic field should be uniform around the body and its value is the one at the center of the body due to the fact that the quadrature birdcage coil configuration was built-in at the center of the body. Therefore, the formulation of transmitted electric field of quadrature birdcage coil model in cylindrical coordinates can be oriented in Eq. (56) as follows:

$$E_z(R) = -\omega\,\mu\,H_-(R=0)\,\mathrm{R} \qquad \textbf{(77)}$$

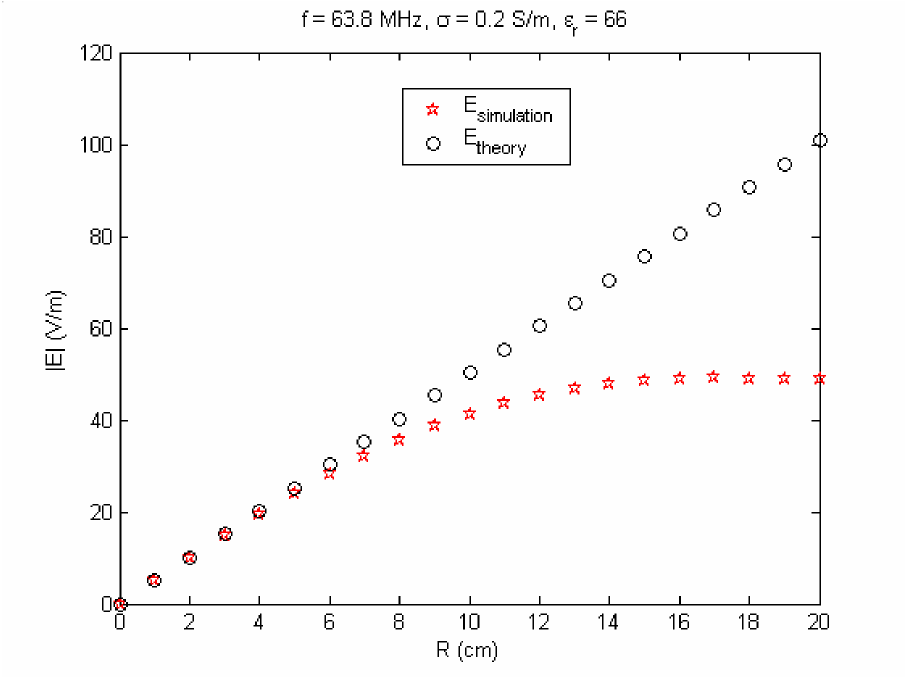

Figure 20. The transmitted RF electric field at 63.8 MHz observed from the quadrature birdcage coil model.

As a consequence, the transmitted electric field was obtained as shown in Figure 20. It is seen that, the theoretical formulation results closely match with the one in the EM simulation at the points close to the center of the body. Whereas, it keeps linearly increasing through the outer points of the body while the simulation results approaches to a steady magnitude.

Considering the phases of the fields, only the phase of the transmitted electric field at the center holds with respect to the referred magnetic field at the center.

4.2.2 Results of Induced Current at the Tip

The simulation results for the effect of the wire length between the case and the bare tip on the induced current at the tip are shown in Figure 21 and Figure 22 for different electromagnetic properties of the medium.

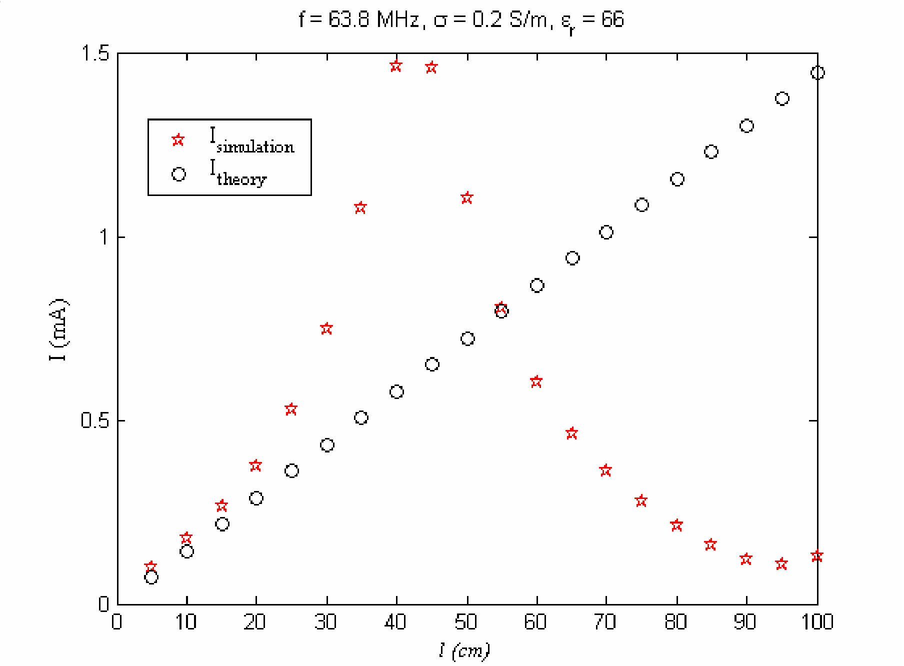

Figure 21. Induced current at 63.8 MHz as a function of wire length, *l*, between the case and the bare tip when the implant is located on R = 6 cm.

According to the plots, while the EM simulation results show resonance effect, the analytical solution linearly increases as a function of the wire length. When the wire length is smaller than the half wave length, the analytical solution closely matches with the EM simulation results. This is because of the quasistatic assumption made at the beginning of the analysis that the size of the implant including its lead was accepted smaller than the wavelength.

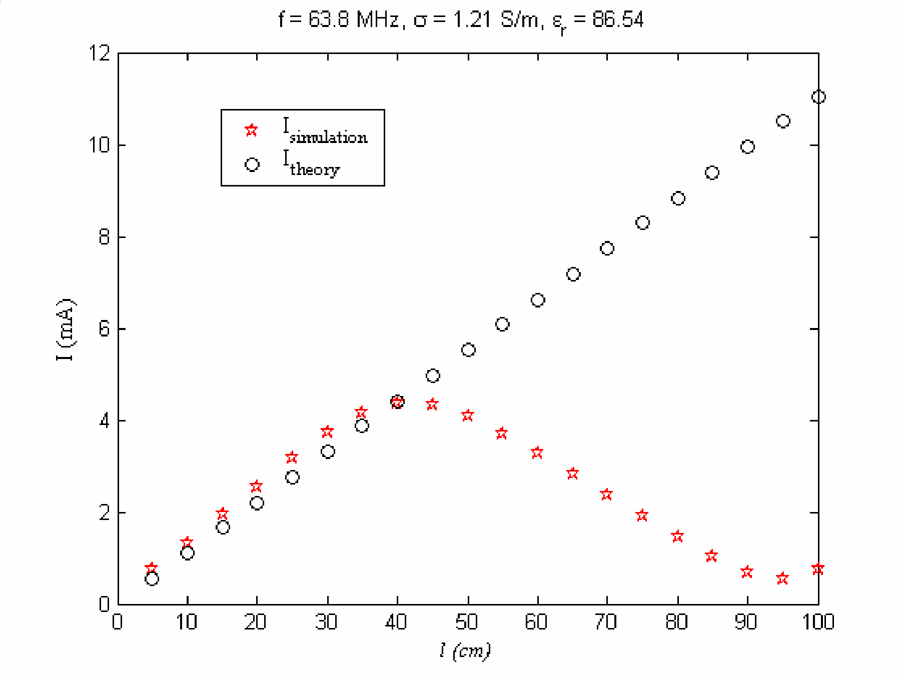

Figure 22. Induced current at 63.8 MHz as a function of wire length, *l*, between the case and the bare tip when the implant is located on R = 6 cm.

Recall that the wavelength in a lossy medium is calculated as the following:

$$\lambda = \frac{2\pi}{\omega\sqrt{\frac{\mu\varepsilon}{2}}\sqrt{1+\left(1+\frac{\sigma^2}{\omega^2\varepsilon^2}\right)^{1/2}}} \qquad \textbf{(78)}$$

This formula gives a wavelength of 53.63 cm for a medium with σ = 0.2 S/m and ε_r = 66. Thus, the half wavelength of this medium is around 26 cm. For another medium, that is blood, with σ = 1.21 S/m and ε_r = 86.54, it is given a wavelength of 31.87 cm with the half wavelength of approximately 15 cm. As it is shown in Figure 21 and 22, both results closely matches when the wire length is smaller than the half wavelength. It should be noted that in Figure 22, both results are very close to each other even when the wire length is longer than the wavelength; this is most probably due to the damping of the system when it has higher electromagnetic properties.

Next, the effect of the implant position inside the cylindrical body was simulated in Figure 23 when the wire length is 10 cm that is smaller than the half wavelength. As can be observed from the plot, as the radial distance from the center increases, the observed current at the tip increases as well for both cases. Considering that RF magnetic field is constant at all radial points but the transmitted electric field increases linearly, the reason behind the rise in current is due to the coupling of the electric field with the straight wire with length *l*, but not the coupling with the transmitted magnetic field.

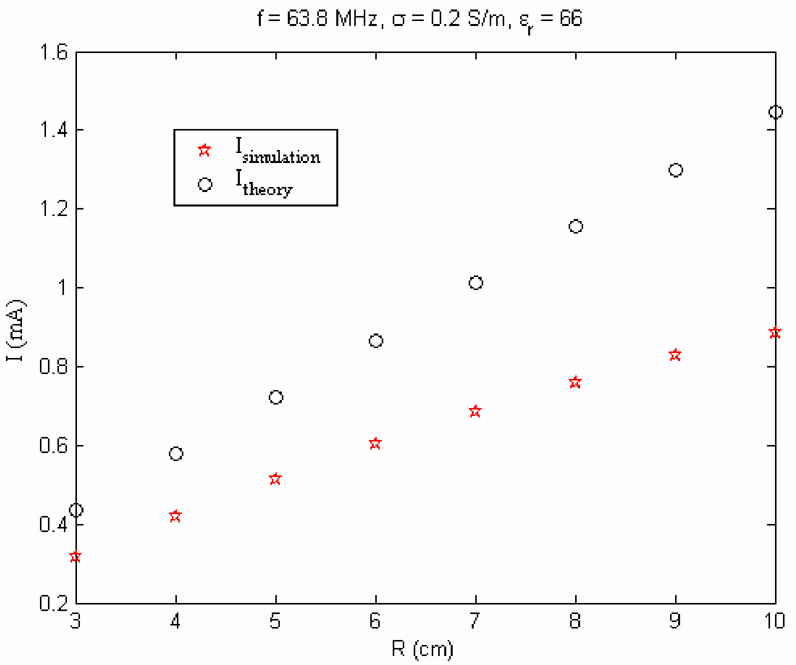

Figure 23. Induced current at 63.8 MHz as a function of R when the wire length, *l*, between the case and the bare tip is equal to 10cm.

Then, the induced current at the tip as a function of the diameter of the tip was simulated in Figure 24. According to Eq.(20), as the diameter of the tip gets larger, the impedance of the tip gets smaller. Therefore, with the increasing diameter the induced current at the tip increases as well.

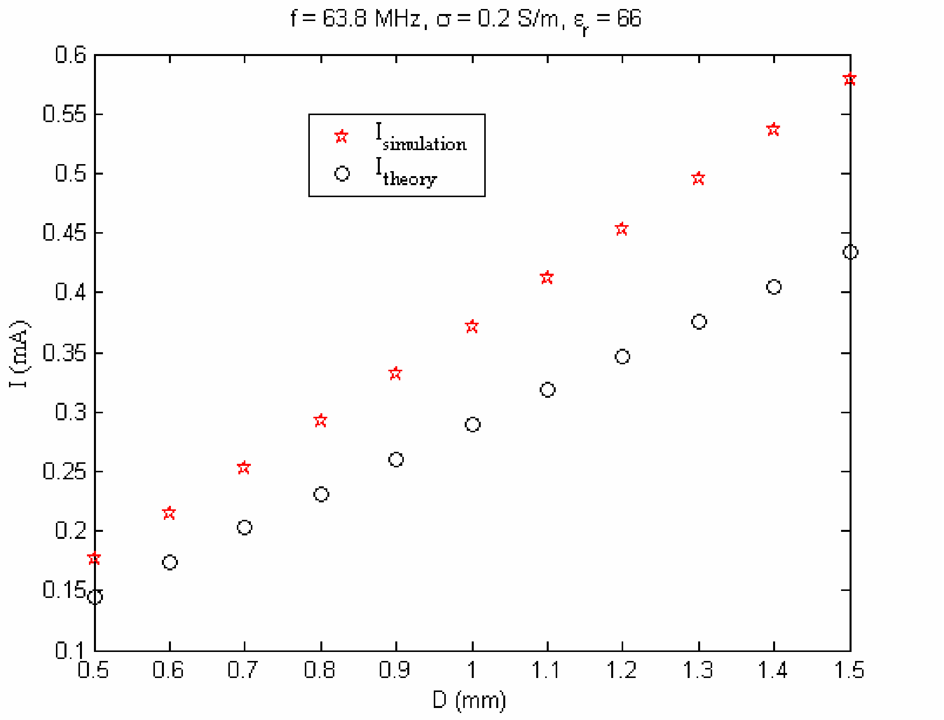

Figure 24. Induced current at 63.8 MHz as a function of the diameter of the tip when the wire length, *l*, is equal to 10 cm and the implant is located at R = 6 cm.

As shown in Figure 25, the induced current at the tip was simulated with respect to the conductivity of the medium. With the rising conductivity of the medium, the impedance of the tip to the medium around decreases depending on the Eq.(20). In this simulation, it is seen that how closely the EM simualtion and the theoretical results match closely.

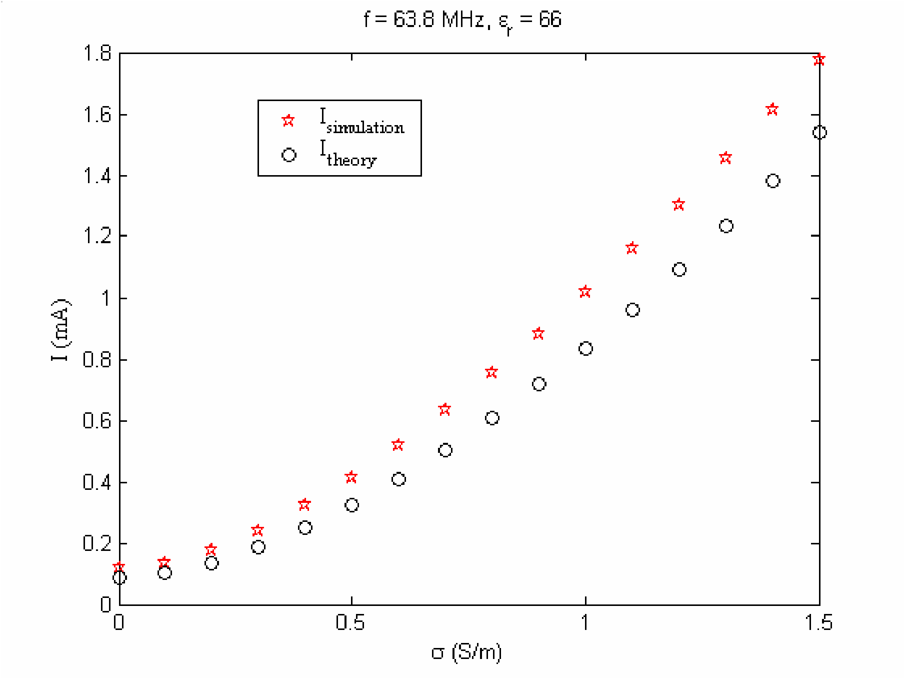

Figure 25. Induced current at 63.8 MHz as a function of the conductivity of the medium when the wire length, *l*, is equal to 10 cm and the implant is located at R = 6 cm.

As the other configuration, the general implant model was approximated as only the curvature of the lead when the wire length is zero. Then, the area of the curvature becomes independent of the wire length so that its effect for the current induction at the tip can be analyzed separately. It should be kept in mind that with that configuration the position of the implant is adjusted according to the center of the loop. First, the area of the curvature was kept constant and the implant was moved in radial direction. Then, the implant was placed at a fixed position, i.e. R = 6 cm, and the area of the lead curvature was changed.

First, in Figure 26 the implant with a constant lead curvature area was moved in the radial direction and the induced current at the tip was measured. Since the transmitted magnetic field assumed to be constant inside the body, it was expected to observe a constant current at the tip no matter the distance of the implant to the center of the body as in the theoretical result in Figure 26.

Contrary to this expectation, in EM simulation results the induced current raises as the distance to center increases. Considering the transmitted electric field distribution of EM simulation in Figure 20, the reason for that increase was thought to be the coupling of the transmitted electric field with the metallic case despite the fact that the wire length between the case and the tip was zero in the simulation. The same amount of current should have been induced to the tip for all R values as the one when R = 0, which is around 43 uA. However, if it is calculated in reverse order by substituting EM simulation data into the formula in Eq.(60), an additional wire length for all data points was observed despite there is no wire between the case and the tip in the simulation. This additional length was thought to be due to the effect of the metallic case height.

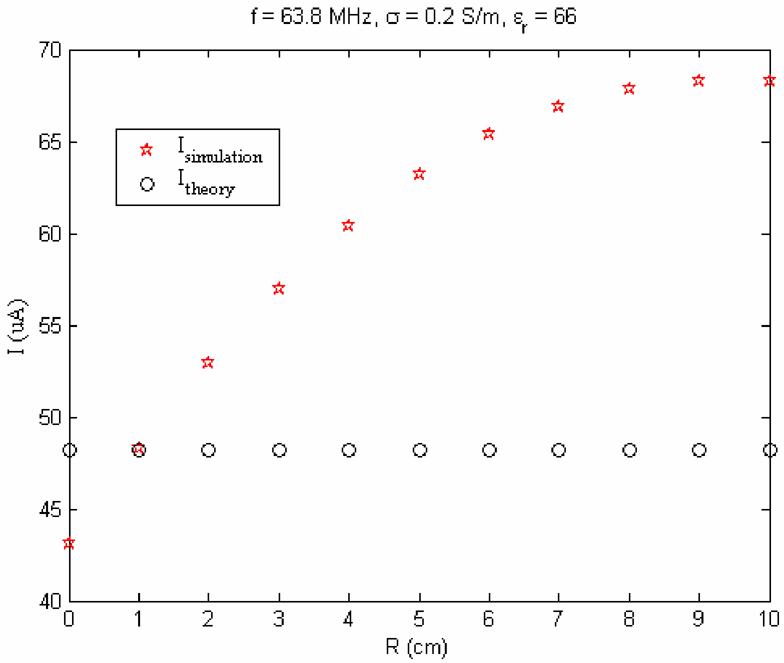

Figure 26. Induced current at 63.8 MHz as a function of R when the area, A, of the curvature is equal to 20 cm^2 when there is no wire between the case and the tip.

The same source of error was observed in Figure 27 as well when the area of the loop was changed without changing the location of the loop center.

When the area of the lead curvature was made wider, the induced current at the tip increases as expected since the coupling of the curvature with the magnetic field gets stronger. However, when it is calculated in the same way done for the previous plot, the same amount of error was observed.

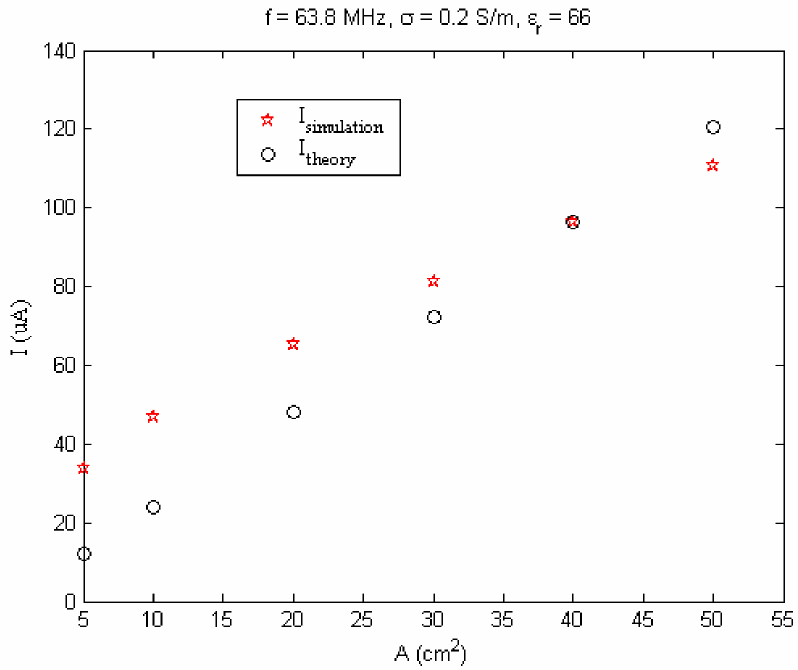

Figure 27. Induced current at 63.8 MHz as a function of area, A, of the curvature when there is no wire between the case and the tip. The center of the curvature is located at R = 6 cm.

In order to eliminate the effect of the metallic case height, the implant configuration was modified in a way that the metallic case was replaced with a wire connected to a sphere, which is the same as the one at the tip, and the area of the loop was conserved with additional wire with 5 cm length as shown in Figure 28. However, with that configuration the impedance of the tip was doubled while in the previous configuration the impedance of the case was negligibly small compared to the tip.

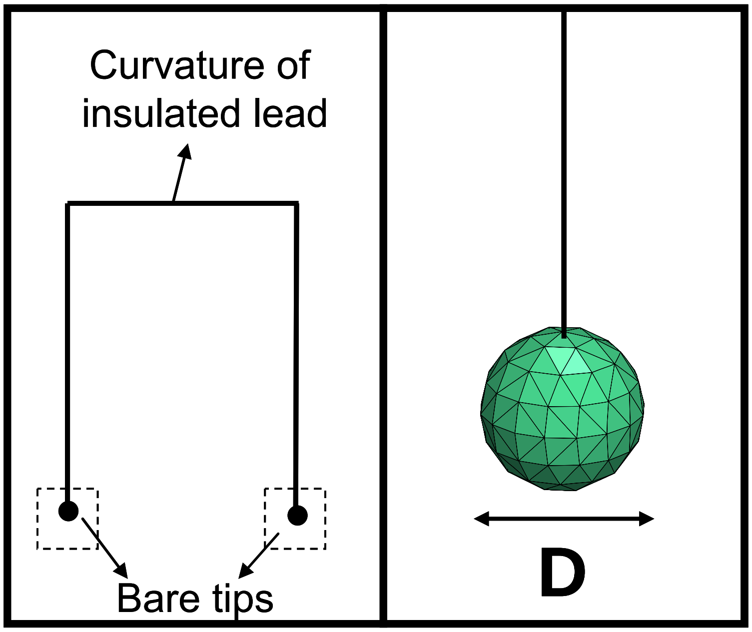

Figure 28. The modified version of implant configuration in Figur, configuration with only curvature of the wire when $l = 0$. There is a sphere at the each side of the lead. Quadrature birdcage coil model was used for the excitation.

With the simplified configuration, it seems in Figure 29 that the source of error can not be eliminated. The reason behind that is the quasistatic assumption assumed at the beginning of the analytical analysis in which the size of the implant was assumed to be significantly smaller than the wavelength; in other words the frequency of the system was assumed to be small. Therefore, we did the same simulation at an extreme case at 63.8 Hz to see the effect of the quasistatic assumption in Figure 30. As a result, a constant current induction at the tip independent of the radial position of the implant was observed.

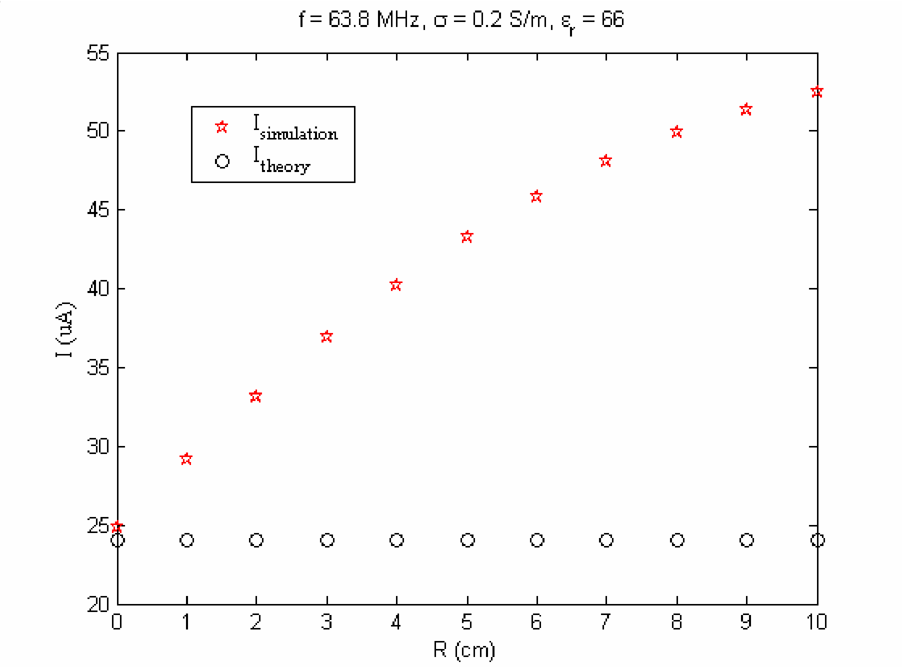

Figure 29. Induced current at 63.8 MHz as a function of R when the case was placed with a wire connected to a sphere, and the area, A, of the curvature is equal to 20 cm^2.

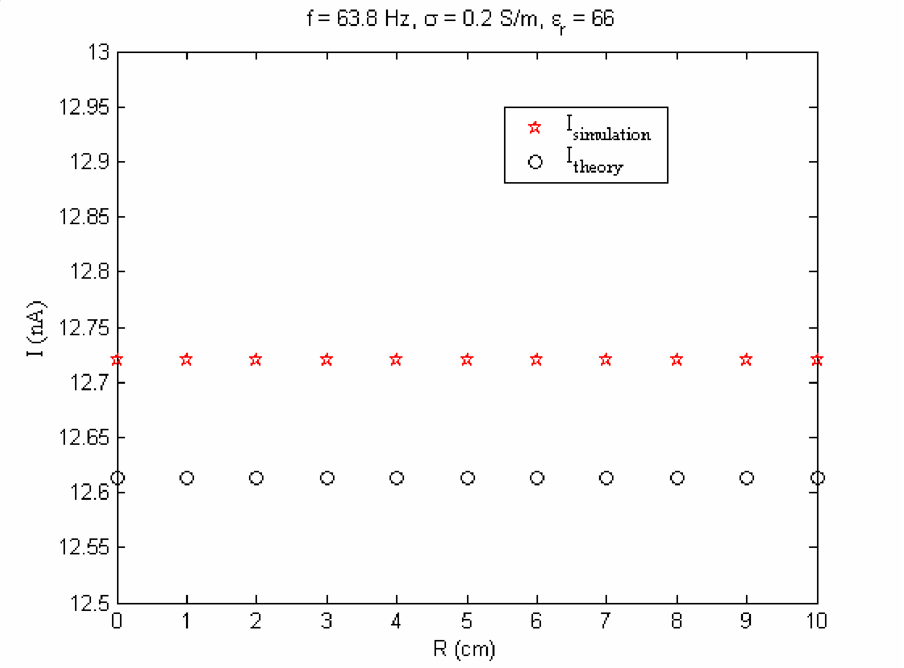

Figure 30. Induced current at 63.8 Hz as a function of R when the case was placed with a wire connected to a sphere, and the area, A, of the curvature is equal to 20 cm^2.

However, even if frequency of 63.8 Hz shows that under quasistatic fields the theoretical analysis matches well with the EM simualtion results; this does not give an intuition about error of the operating frequency, 63.8 MHz. Therefore, the simulation for other lower frequencies but in MHz order at critical data points was repeated. The obtained plots are shown in Figure 31 with the estimated maximum errors that are obtained at R = 10 cm were displayed in Table 4

Table 4. Estimated errors of induced current at the tip at different frequencies when the case was placed with a wire connected to a sphere, and the area, A, of the curvature is equal to 20 cm^2.

f (MHz)	I_{theory} (μA)	$I_{simulation}$ (μA) at R = 10 cm	Estimated Maximum Error (%)
63.8	24.07	52.51	118.12
10	5.12	8.59	67.82
5	3.55	4.44	24.9
1	1.58	1.61	1.99

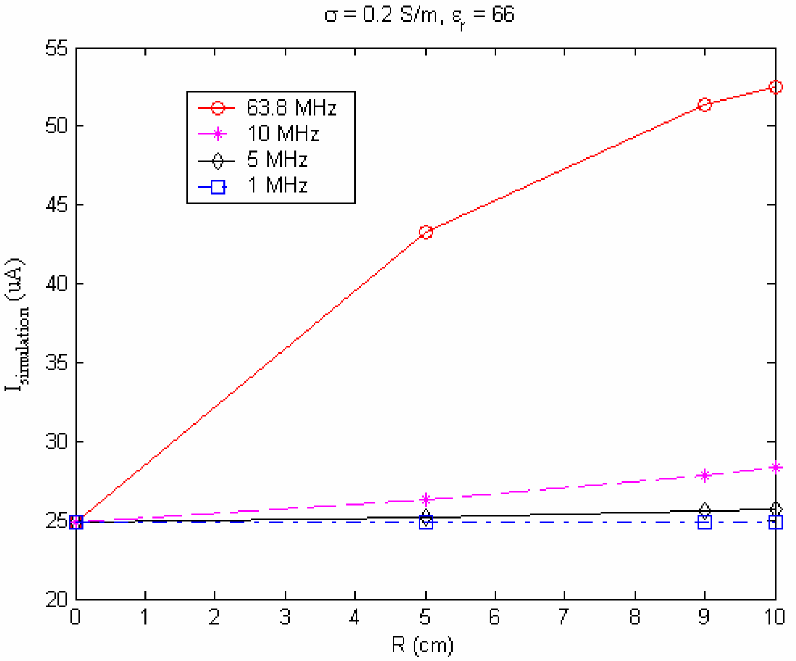

Figure 31. Induced current at different frequencies as a function of R when the case was placed with a wire connected to a sphere, and the area, A, of the curvature is equal to 20 cm^2. The results were normalized with respect to the 63.8 MHz data.

As shown in Table 4, at 63.8 MHz the estimated error was calculated as 118.12%, while at 10 MHz the estimated error was reduced by half. At 5 MHz and 1 MHz the estimated errors can be acceptable; therefore, these frequencies and lower ones can be in the quasistatic frequency range.

In Figure 32, the induced current as a function of area with the configuration of two spheres connected with a wire was plotted. This time the slopes of the both data match.

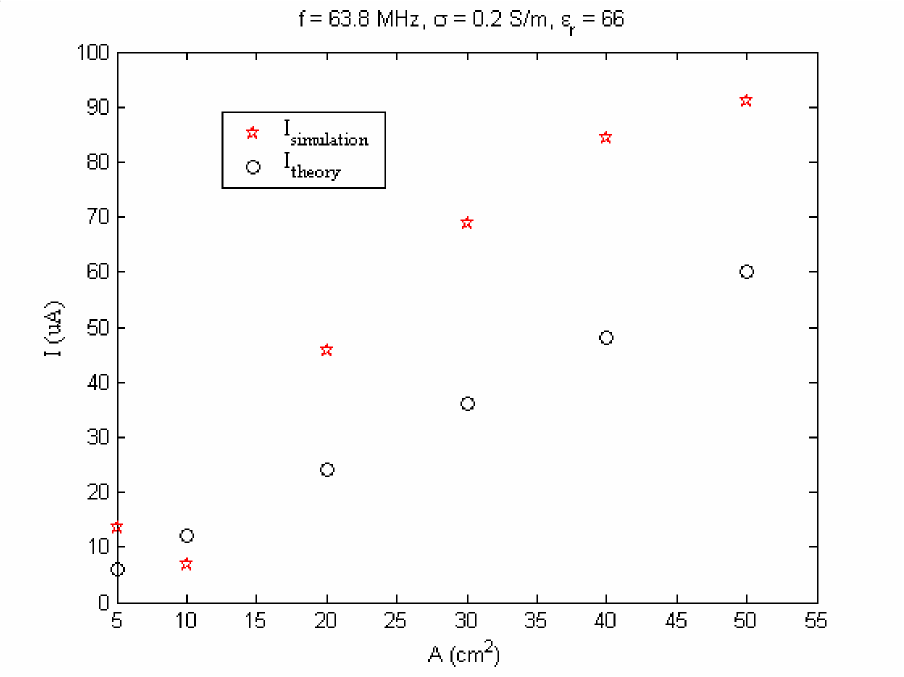

Figure 32. Induced current at 63.8 MHz as a function of area, A, of the curvature the case was placed with a wire connected to a sphere. The center of the curvature is located at R = 6 cm.

The most primitive configuration of an implant with the curved lead is a loop of wire of which one segment is loaded with the impedance of the tip as shown in Figure 33. In that configuration, the impedance of the spherical tip was calculated and added to the loop of wire. The simulation result is shown in

Figure 34. According to the EM simulation data with this configuration, the coupling of the loop with the magnetic field decreases as the loop gets further away in radial direction. This is because the magnetic field in the EM simulation decreases as a function of radial distance from the center of the body as shown in Figure 19. If the induced current data obtained at the center of the body in Figure 33 was considered (since we use the magnetic field value at the center of the body in the quadrature birdcage field model), the theoretical data calculated is very close to the EM simulation data as expected.

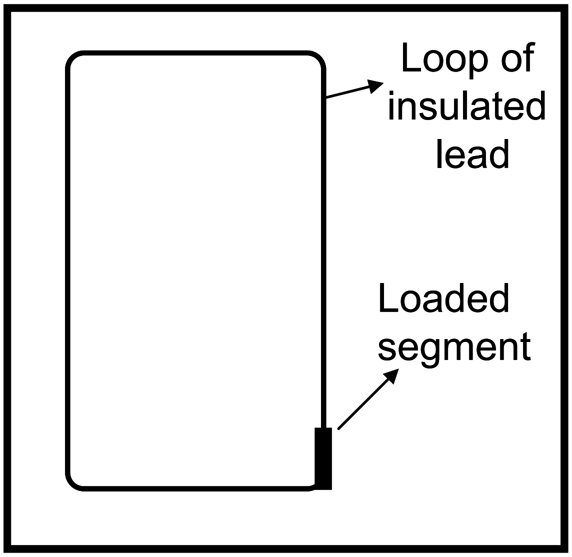

Figure 33. The most primitive version of implant configuration in Figure 12, configuration with a wire of loop that shown segment was loaded with the impedance of the tip. Quadrature birdcage coil model was used for the excitation.

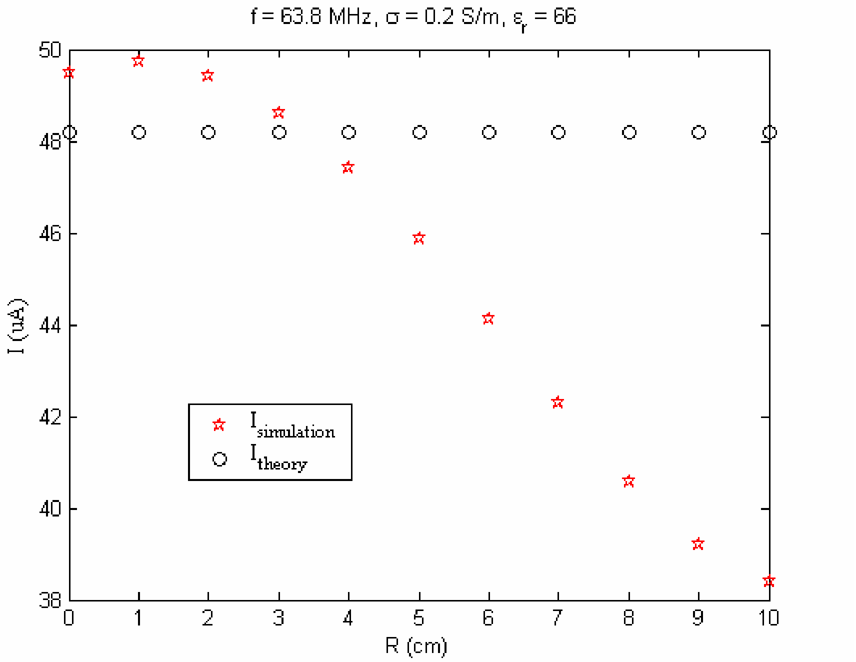

Figure 34. Induced current on a loop of wire whose one of the segments loaded with the impedance e of the tip as a function of R. the area of the loop is equal to 20 cm^2.

4.2.3 Results of Gel Phantom Simulation

The use of cylindrical phantom container with a limited length is the most important confliction of the real life with the theory. Therefore, before the experiment, the points where the eddy currents can be detected best should be determined. Since eddy current induction is directly related to the transmitted electric field, the electric field distribution inside the gel phantom gave the necessary insight for the experiment, i.e. where to place the probes inside the gel to obtain a reasonable data.

Besides, this simulation enabled to determine the accuracy of the quadrature birdcage coil model. Because, the quadrature birdcage coil model was developed by assuming an infinitely long cylindrical human model. It is important to estimate the amount of error in the transmitted electric field distribution when the same excitation is used with a geometry that is limited in size.

As it is seen in Figure 35, if we place the fiber optic temperature probes very close to either the bottom or top ends, the electric field, consequently SAR, decreases as going away from the center contrary to it should increase. Therefore, it should be poured a gel with enough height to prevent probes from being very close to the bottom or top of the container.

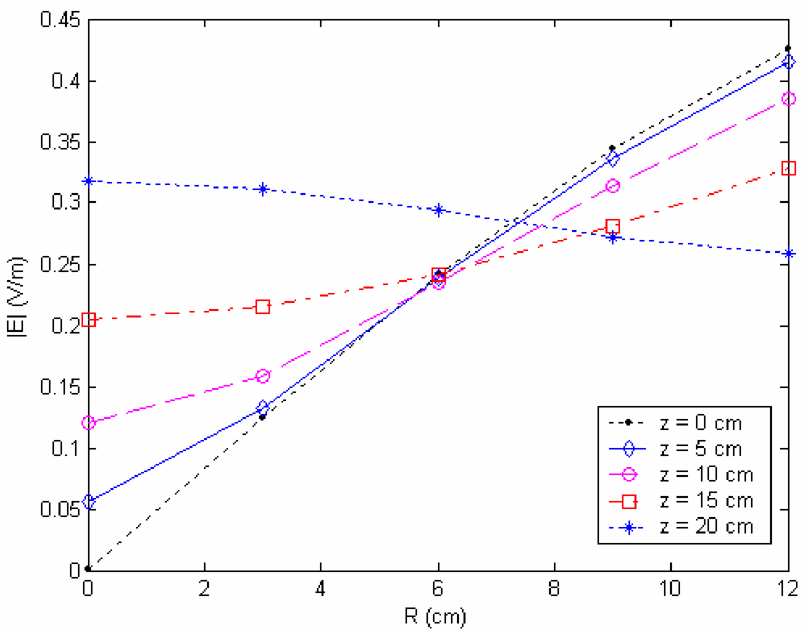

Figure 35. Transmitted electric field distribution inside a cylindrical gel phantom at the center, and the height of 5 cm, 10 cm, 15 cm and 20 cm.

For other heights, through the center of the phantom the intensity of fields increases, but it is stronger between 10 cm and 15 cm.

A gel that heights 24 cm was prepared, and the probes were placed at 4 cm depth from the top of the gel. Therefore, the simulation results for the electric field distribution inside the gel phantom at z = 10 cm can give a useful insight about the deposited power in the gel in advance the phantom experiment is performed.

Table 5. The transmitted field results of gel phantom inside the quadrature birdcage coil model in the EM simulation. However, SAR is calculated by hand using Eq.(1)

R (cm)	$\|E\|$ (V/m)	$\|H_-\|$ (F/m)	SAR (µW/kg)
0	0.056	0.0137	0.63
3	0.132	0.0134	3.48
6	0.239	0.0125	11.42
9	0.336	0.011	22.58

So as to calculate the corresponding transmitted electric field using Eq.(56), the RF magnetic field value at the center should be used but normalized with $\sqrt{2}$ as explained in section 3.3.1. That is $H_-(R = 0) / \sqrt{2} = 0.0097$ A/m. Then the resultant transmitted electric field and the SAR values are displayed in Table 6.

Table 6. The calculated transmitted field and resulted SAR values for the gel phantom inside the quadrature birdcage coil model.

R (cm)	$\|E\|$ (V/m)	SAR (µW/kg)
0	0	0
3	0.147	4.32
6	0.294	17.29
9	0.441	38.9

As you seen in Table 7, the simulated SAR does not increase quadratically as a function of R while the theoretical SAR does. Besides, the percentage of the estimated error increases as going away from the center of the body. That result is consistent with the transmitted electric field results shown in Figure 20.

Table 7. The estimated error between the EM simulation data and the theoretical data

R (cm)	**SAR$_{simulation}$ (µW/kg)**	**SAR$_{theory}$ (µW/kg)**	**Estimated Error (%)**
0	0.63	0	-
3	3.48	4.32	19.44
6	11.42	17.29	33.95
9	22.58	38.9	41.95

4.3 Experiment Results

The theoretical SAR values calculated for the specified locations are shown in Table 8 using the transmitted electric field formula of quadrature birdcage coil model in Eq.(56) and SAR formula for rms electric field in Eq.(1) for comparison with the experimental results.

Table 8. The calculated theoretical SAR values

R (cm)	**Theoretical SAR (W/kg)**
3	1.77
6	7.08
9	15.94

One of the experimental data is shown in Figure 36 for experiment 2. After the linear fitting of the data between the start and end time of the experiment, the baseline SAR was calculated by calorimetry.

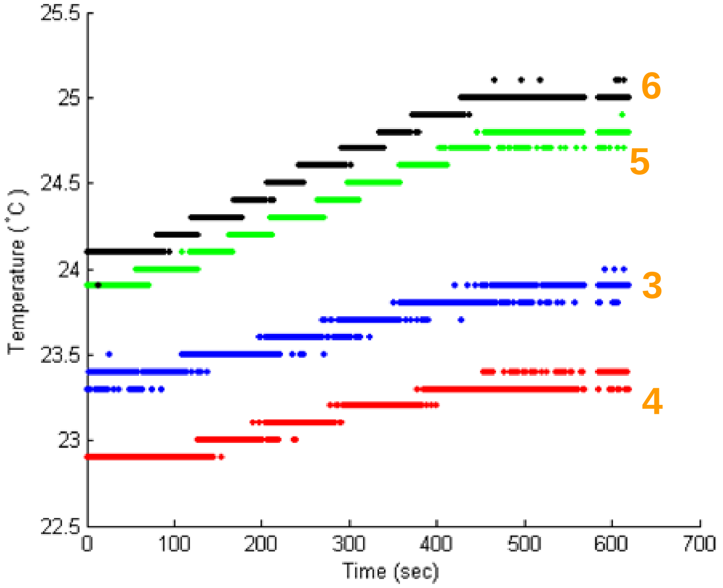

Figure 36. One of the typical experimental data. This is the data of the experiment 2 with probes 3, 4, 5 and 6.

As a result of the first experiment, the results displayed in Table 9 were obtained. Probes 1 and 2 should measure similar temperature values since they are located at equal distances from the center of the phantom while probes 5 and 6 should detect much more than them. Even if obtained data is reasonable considering the positions of probes with respect to each other, only probe 2 observes a good data considering the theoretical data.

Table 9. Results of experiment 1 with probes 1, 2, 5, and 6

Experiment 1 Probe No	Experimental SAR (W/kg)	Estimated Error (%)
1	2.98 - 3.42	40.51 - 48.28
2	1.6 - 1.8	1.84 - 11.02
5	7.51 - 7.65	108.37 - 112.23
6	8.23 - 8.42	89.42 - 93.72

In the second experiment, while probe 3 should detect similar results with probe 4, probe 5 should do with probe 6. Considering data of the first experiment, data of probes 3 and 4 is reasonable with respect to probes 1 and 2. Notice that probes 5 and 6 get similar values for both experiments.

Table 10. Results of experiment 2 with probes 3, 4, 5, and 6

Experiment 2 Probe No	Experimental SAR (W/kg)	Estimated Error (%)
3	4.31 - 4.57	55.09 - 64.17
4	4.23 - 4.43	59.83 - 67.58
5	7.41 - 7.61	109.47 - 115.27
6	8.53 - 8.75	82.28 - 86.9

In the third experiment, a quite good data was observed considering the analytical values in Table 8.

Table 11. Results of experiment 3 with probes 1, 2, 3, and 4

Experiment 3 Probe No	Experimental SAR (W/kg)	Estimated Error (%)
1	2.7 - 2.84	34.37 - 37.62
2	1.83 – 2.0	3.26 - 11.57
3	5.28 - 5.53	34.21 - 28.07
4	6.21 - 6.49	9.14 - 14.1

The experiments 4, 5 and 6 give also good results.

Common to all probes placed at 9cm away from the center of the phantom, i.e. probes 5, 6 and 8, the estimated percentage of error are much larger than it can be accepted. The reason for that is the difference with the theory (developed for an infinitely long cylindrical human body model) and the experiment (done with a cylindrical phantom container with limited size).

Table 12. Results of experiment 4 with probes 2, 3, 4, and 6

Experiment 4 Probe No	**Experimental SAR (W/kg)**	**Estimated Error (%)**
2	2.47 - 2.9	28.17 - 38.91
3	4.45 - 4.57	54.84 - 59.04
4	4.59 - 4.71	50.5 - 54.22
6	9.05 - 9.29	71.57 - 76.23

Table 13. Results of experiment 5 with probes 4, 7, 8, and 9

Experiment 5 Probe No	**Experimental SAR (W/kg)**	**Estimated Error (%)**
4	4.46 - 4.63	52.88 - 58.65
7	4.03 - 4.16	70.24 - 75.97
8	8.36 - 8.58	85.86 - 90.66
9	4.5 - 4.64	52.64 - 57.23

Table 14. Results of experiment 6 with probes 3, 4, 7, and 8

Experiment 6 Probe No	**Experimental SAR (W/kg)**	**Estimated Error (%)**
3	4.72 - 4.88	45.19 - 50.03
4	4.18 - 4.31	64.45 - 69.64
7	4.07 - 4.19	68.9 - 74.23
8	9.17 - 9.41	69.37 - 73.9

Chapter 5

Discussion

In this thesis, the safety index of AIMDs, that is the maximum temperature increase at the tip of the implant as a result of unit applied SAR, has been analytically solved for known RF magnetic and transmitted electric field distribution. Throughout the analytical analysis, some simplifying assumptions had to be done to obtain a comprehensible and practical formulation that illustrates the effect of each parameter on the RF heating of AIMDs. Mentioning these assumptions once more is beneficial to discuss on their use during the design and limitations in the application of the safety index formula.

- This solution was derived under the quasistatic assumption. In other words, the size of the implant was assumed to be smaller than the half wavelength. Considering the implant configuration, length of the lead is the main component determining the size of the implant; therefore it can be concluded that this solution is valid for short leads. With short leads, it is meant to be leads shorter that 20 cm. Therefore, this analysis is valid for wires with length less than half wavelength. The safety index formulation derived is not suitable for most implants since the typical lead lengths are longer than 20 cm ranging 50-80 cm. The results obtained in this thesis are the first steps toward understanding longer lead lengths. We have started working on transmission line model in order to understand the current distribution on longer leads.

- The quasistatic assumption was helpful to reduce the number of variables contributing the RF heating of the AIMDs so that more effective parameters can be analyzed effectively.

- The operating frequency of safety index formulation is 63.8 MHz. The same RF heating model can be applied for higher field strengths, but the solution should be revised and tested at these frequencies. At 63.8 MHz, the homogeneity of fields was the main advantage and it was possible to take use of quasistatic assumption. At higher field strengths, the field homogeneity and wavelength decreases, therefore it is more complicated to derive the safety index of implants at higher frequencies.

- An alternative safety index formulation was proposed for an analytical model of the RF electric field transmitted by a quadrature birdcage coil. This solution presents a more compact formulation. The proposed quadrature birdcage coil model is the first model in the literature. For other body coil designs, the safety index formulation should be developed by relaying on the constraints of the body coil.

- The assumption of the bare tip as a spherical conductor while the insulated lead was assumed very thin enabled to use it as a point source during the Green's function averaging technique to find the temperature distribution in the tissue.

- During the analysis, body thermal and electrical properties were assumed to be constant around the tip. Because, local heating occurs in a small region of interest and away from any boundaries. This assumption made the use Green's function averaging technique possible during the analysis.

- In this thesis, the safety index formulation was derived for only an AIMD with a single lead. There are also AIMDs with multi-leads. For these implants, the safety index formulation should be modified considering the configuration of all leads in the human body.

The perfusion correction factor approaches 1 as perfusion and the lead diameter decrease. Note that, for typical values of the lumped perfusion parameter (less than 0.5 mm^{-1}) and the lead tip diameters (1 mm), this correction factor is between 0.5 and 1. Therefore, one can use $f(Dv)$ as equal to 1 if a perfusion independent, worst case safety index value is desired.

On the other hand, the body thermal parameters used in safety index formulation, α and c_t can be found in literature and used in this equation. Phantom experiments needs to be carried out with care since phantom (gel) and body thermal parameters may not match.

The safety index formulation illustrates that the RF tip heating of an implant depends on the way the loop made and the position of the implant in the body. The angle of the loop with the radial axis has a significant effect on the RF heating of the tip. The worst angle is 0°, in that Rl and A terms add up and give rise to maximum heating. On the other hand, minimum heating occurs when this angle is 180° as shown in Figure 37. Note that this angle depends on how implant is placed in the body. The way the loop made also determines this angle because the direction of current changes depending on whether the lead is looped clockwise or counter-clockwise. With the changed current flow, the direction of loop normal changes, so the angle between the loop and the radial axis is altered as well.

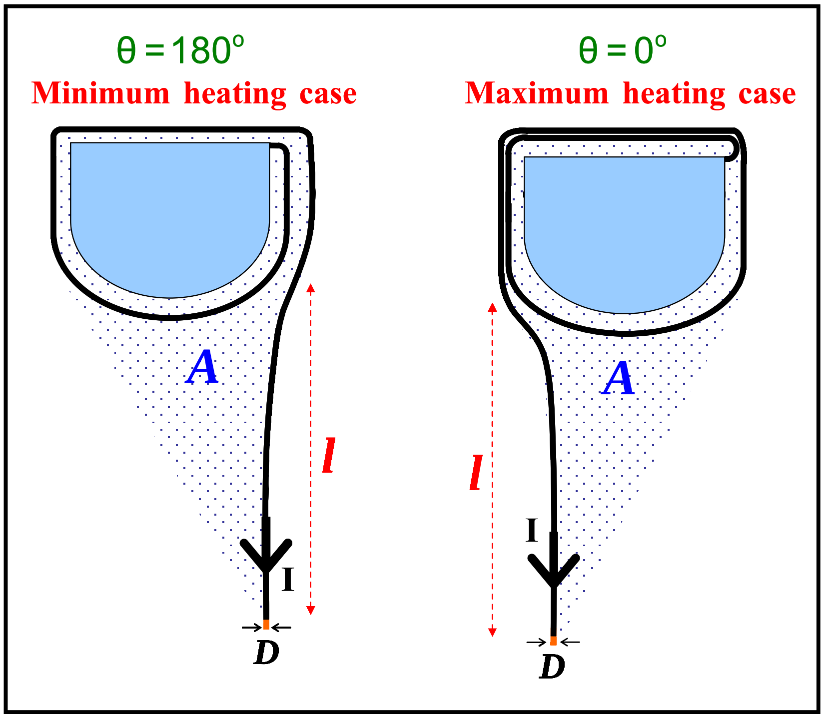

Figure 37. Two different configurations may result in significantly different heating at the tip. Right panel shows the maximum heating configuration.

For the sake of obtaining some numerical values, if the perfusion correction factor is ignored and a small area of the loop was assumed, and use the thermal parameters ($\alpha = 1.3\text{x}10\text{-}7\ \text{m}^2/\text{sec}$ and $c_t = 3662$ J/kg/°C) measured, a very simple expression $\text{SI} = 0.017\ l^2$ would be obtained where l is given in cm when the implant is located at a 6 cm away from the center of the body whose radius is 15 cm. In other words, while 1 cm lead would not cause any significant heating, a 20 cm lead heats up to approximately 7°C when it is exposed to 1 W/kg SAR.

The safety index estimates the maximum temperature increase when there is an active implant in the tissue per unit applied SAR without the implant in place. The safety index formulation ensures the RF safety of an implant by limiting the SAR of the applied RF field. This easy to understand formulation enables to combine the MRI scanner estimated SAR that does not take into account of the existence of an implant with a contradictory situation scanning of a patient with an implant. This stress on the fact that scanner calculated SAR is an important parameter for the safety of implants.

Chapter 6

Conclusion and Future Work

To sum up, the RF heating of active implants during MRI scans was formulated with a simple formula such that it is very easy to foresee how much temperature rise can occur at the tip of the implant lead during MRI exam. By adjusting power level of pulse sequences, patient can be scanned safely.

First, the induced current and safety index formula was derived for active implants assuming a known RF electric and magnetic field distribution. Then, a quadrature birdcage coil model was developed for estimating the transmitted electric field distribution from a known RF magnetic field. The analytical solution of circular waves, simulation and experimental results showed that this model is a good analytical approximation of the incident electric field distribution inside an infinitely long cylindrical human model. Relying on that birdcage coil model, the induced current at the tip and safety index formula was modified. In order to understand the effects of wire length and the loop area on the induced current at the tip, the simulations of the induced current at the tip was done. Results of the simulations and analytical induced current formula showed that the analytical formulation is a good approximation of the RF heating phenomenon especially for wire lengths smaller than the half wavelength.

However, experimental verification of the safety index with gel phantom needs to be done to ensure the validity of the safety index formulation as a future work. As it is done in simulations, first loop of the implant can be neglected and only the safety index of a straight insulated wire with bare tip connected to a metallic case can be measured. Then, the same can be done with only loop of wire without any wire length between the bare tip and the case.

BIBLIOGRAPHY

1. Achenbach, S., et al., *Effects of magnetic resonance imaging on cardiac pacemakers and electrodes.* Am Heart J, 1997. **134**: p. 467-473.
2. Chou, C., J.A. McDougall, and K.W. Chan, *RF heating of implanted spinal fusion stimulator during magnetic resonance imaging.* IEEE Trans Biomed Eng, 1997. **44**(5): p. 367-373.
3. Rezai, A.R., et al., *Neurostimulation systems for deep brain stimulation: in vitro evaluation of magnetic resonance imaging-related heating at 1.5 tesla.* J Magn Reson Imaging, 2002. **15**: p. 241-250.
4. Luechinger, R., et al., *In vivo heating of pacemaker leads during magnetic resonance imaging.* Eur Heart J, 2005. **26**: p. 376-383.
5. Sommer, T., et al., *MR imaging and cardiac pacemakers: in vitro evaluation and in vivo studies in 51 patients at 0.5 T.* Radiology, 2000. **215**: p. 869-879.
6. Yeung, C.J., R.C. Susil, and E. Atalar, *RF safety of wires in interventional MRI: using a safety index.* Magn Reson Med, 2002. **47**: p. 187-193.
7. Park, S.M., et al., *MRI Safety: RF-induced heating near straight wires.* IEEE Trans Magn, 2005. **41**(10): p. 4197-4199.
8. Smith, C.D., et al., *Interactions of magnetic resonance imaging radio frequency magnetic fields with elongated medical implants.* J Appl Phys, 2000. **87**(9): p. 6188-6190.
9. Nyenhuis, J.A., et al., *MRI and implanted medical devices: basic interactions with an emphasis on heating.* IEEE Trans Device Mater Rel, 2005. **5**(3): p. 467-480.
10. Luechinger, R., *Safety aspects of cardiac pacemakers in magnetic resonance imaging*, in *Dept. Naturwissenschaften*. 2002, Swiss Federal Inst Technol: Zurich, Switzerland.
11. Baker, K.B., et al., *Reduction of magnetic resonance imaging-related heating in deep brain stimulation leads using a lead management device.* Neurosurgery, 2005. **57**: p. 392-396.
12. Bassen, H., et al., *MRI-induced heating of selected thin wire metallic implants - laboratory and computational studies - findings and new questions.* Minim Invasiv Ther, 2006. **15**(2): p. 76-84.
13. Spiegel, J., et al., *Transient dystonia following magnetic resonance imaging in a patient with deep brain stimulation electrodes for the treatment of Parkinson disease.* J Neurosurgery, 2003. **99**: p. 772-774.
14. Baker, K.B., et al., *Evaluation of specific absorption rate as a dosimeter of MRI-related implant heating.* J Magn Reson Imaging, 2004. **20**: p. 315-320.
15. Baker, K.B., et al., *Variability in RF-induced heating of a deep brain stimulation implant across mr systems.* J Magn Reson Imaging, 2006. **24**: p. 1236-1242.

16. Rezai, A.R., et al., *Is magnetic resonance imaging safe for patients with neurostimulation systems used for deep brain stimulation?* Neurosurgery, 2005. **57**(5): p. 1056-1060.
17. Rezai, A.R., et al., *Neurostimulation system used for deep brain stimulation (DBS): MR safety issues and implications of failing to follow safety recommendations.* Invest Radiol, 2004. **39**(5): p. 300-3003.
18. Nitz, W.R., et al., *Specific absorption rate as a poor indicator of magnetic resonance-related implant heating.* Invest Radiol, 2005. **40**(12): p. 773-776.
19. Bottomley, P.A. and E.R. Andrew, *RF magnetic field penetration, phase shift and power dissipation in biological tissue: implications for nmr imaging.* phys med biol, 1978. **23**(4): p. 630-643.
20. Atalar, E., *Radiofrequency safety for interventional MRI procedures.* Acad Radiol, 2005. **12**: p. 1149-1157.
21. Yeung, C.J. and E. Atalar, *Green's function approach to local rf heating in interventional MRI.* Med Phys, 2001. **28**(5): p. 826-832.
22. Pennes, H.H., *Analysis of tissue and arterial temperatures in the resting human forearm.* J Appl Phys, 1948. **1**: p. 93-122.
23. Glover, G.H., et al., *Comparison of linear and circular polarization for magnetic resonance imaging.* J Magn Reson, 1985. **64**: p. 255-270.
24. Bottomley, P.A., et al., *Estimating radiofrequency power deposition in body NMR imaging.* Magn Reson Med, 1985. **2**: p. 336-349.
25. Foo, T.K., C.E. Hayes, and Y. Kang, *An analytical model for the design of rf resonators for MR body imaging.* Magn Reson Med, 1991. **21**: p. 165-177.
26. Reilly, J.P. and A.M. Diamant, *Theoretical evaluation of peripheral nerve stimulation during MRI with an implant spinal fusion stimulator.* Magn Reson Imaging, 1997. **15**(10): p. 1145-1156.
27. Luechinger, R., et al. *Heat distribution near pacemaker lead tips*. in *In: Proceedings of 9th Annual Meeting of ISMRM*. 2001. Glasgow, Scotland.
28. Angelone, L.M. and G. Bonmassar. *Effect of deep brain stimulation lead resistivity on specific absortion rate at 3 T mri*. in *Proc. Intl. Soc. Mag. Reson. Med. 15*. 2007. Berlin, Germany.
29. Gao, B., S. Langer, and P.M. Corry, *Application of time-dependent Green's function and Fourier transforms to the solution of the bioheat equation.* Int J Hyperthermia, 1995. **11**(2): p. 267-285.
30. Chen, J., Z. Feng, and J. Jin, *Numerical simulation of SAR and B1-field inhomogenity of shielded RF coils loaded with the human head.* IEEE Trans Biomed Eng, 1998. **45**(5): p. 650-659.
31. Hayes, C.E., et al., *An efficient, highly, homogeneous radiofrequency coil for whole-body NMR imaging at 1.5 T.* J Magn Reson, 1985. **63**: p. 622-628.
32. Jin, J. and J. Chen, *On the SAR and field inhomogenity of birdccage coils loaded with the human head.* Magn Reson Med, 1997. **38**: p. 953-963.

33. Collins, C.M., S. Li, and M.B. Smith, *SAR and B1 field distributions in a heterogenous human head model within a birdcage coil.* Magn Reson Med, 1998. **40**: p. 847-856.
34. Collins, C.M. and M.B. Smith, *Calculations of B1 distirbution, SNR, and SAR for a surface coil adjacent to an anatomically-accurate human body model.* Magn Reson Med, 2001. **45**: p. 692-699.
35. Yeung, C.J., R.C. Susil, and E. Atalar, *RF heating due to conductive wires during MRI depends on the phase distribution of the Transmit Field.* Magn Reson Med, 2002. **48**: p. 1096-1098.
36. Cheng, D.K., *Field and Wave Electromagnetics*. Second ed. 1989: Addison-Wesley Publishing Company, Inc.
37. Celik, H., et al., *Evaluation of internal MRI coils using ultimate intrinsic SNR.* Magn Reson Med, 2004. **52**: p. 640-649.
38. http://www.fcc.gov/fcc-bin/dielec.sh.
39. Ferhanoglu, O., *Safety of Metallic Implants for Magnetic Resonance Imaging*, in *Department of Electrical and Electronics Engineering*. 2005, Bilkent University: Ankara. p. 37-40.
40. Hirata, A., O. Fujiwara, and T. Shiozawa, *Correlation between peak spatial-average SAR and temperature increase due to antennas attached to human trunk.* IEEE Trans Biomed Eng, 2006. **53**(8): p. 1658-1664.
41. http://kurslab.fysik.lth.se/FED4Medopt/bioheatequation.pdf.
42. Brix, G., et al., *Estimation of heat transfer and temperature rise in partial-body regions during MR procedures: An analytical approach with respect to safety considerations.* Magn Reson Imaging, 2002. **20**: p. 65-76.
43. Collins, C.M., et al., *Temperature and SAR calculations for a human head within volume and surface coils at 64 and 300 MHz.* J Magn Reson Imaging, 2004. **19**: p. 650-656.
44. Nguyen, U.D., et al., *Numerical evaluation of heating of the human head due to magnetic resonance imaging.* IEEE Trans Biomed Eng, 2004. **51**(8): p. 1301-1309.
45. http://www.gehealthcare.com/gecommunity/mri/ortho/ortho_apps-techniques1-2-10.html.
46. Dwight, H.B., *Tables of integrals and other mathematical data*. 1961, New York: Macmillan Publishing Co., Inc. pp. 224-225, 234.

APPENDIX

Fourier Transform

The following Fourier Transform convention is used in our derivations;

$$F(v_x) = \int_{-\infty}^{\infty} f(x) e^{iv_x x} dx \qquad \textbf{(79)}$$

$$f(x) = \frac{1}{2\pi} \int_{-\infty}^{\infty} F(v_x) e^{-iv_x x} dv_x \qquad \textbf{(80)}$$

where $v_x = 2\pi k_x$, x is the distance in space domain and k_x is the distance in Fourier domain.

Depending on that convention, Fourier and inverse Fourier Transform of the spherically symmetric objects is calculated as follows (reference?);

$$F(q) = \int_0^{\infty} f(r) \frac{\sin(qr)}{qr} 4\pi r^2 dr \qquad \textbf{(81)}$$

$$f(r) = \frac{1}{(2\pi)^3} \int_0^{\infty} F(q) \frac{\sin(qr)}{qr} 4\pi q^2 dq \qquad \textbf{(82)}$$

where r and q are the radial distance away from the center of the sphere in space and Fourier domain respectively.

Convolution Property gives

$$f(r) * g(r) \overset{FT}{\leftrightarrow} F(q)G(q) \qquad \textbf{(83)}$$

Special Integral Identities

We take advantage of some of the integral relationships from [46], which are listed below, in our calculations;

$$\int_0^{\infty} e^{-ax} \sin(mx) dx = \frac{m}{a^2 + m^2} \quad \text{for } a \geq 0 \qquad \textbf{(84)}$$

$$\int_0^{\infty} \frac{\cos(mx)}{a^2 + x^2} dx = \frac{\pi}{2a} e^{-ma} \quad for \quad a > 0 \quad and \quad m \geq 0 \qquad \textbf{(85)}$$